A NEXT GENERATION THERANOSTIC NANO-PLATFORM FOR SUSTAINED AND ENHANCED INHIBITION OF CANCER STEM CELLS

BY

FATEMEH OSTADHOSSEIN

THESIS

Submitted in partial fulfillment of the requirements
for the degree of Master of Science in Bioengineering
in the Graduate College of the
University of Illinois at Urbana-Champaign, 2015

Urbana, Illinois

Adviser:

Professor Dipanjan Pan

ABSTRACT

Primary tumor extermination and conventional chemotherapy are proved to be inefficient in cancer therapy in that they preferentially abolish differentiated cells whilst leaving behind treatment resistant, tumorigenic cancer stem cells (CSCs). CSCs are validated to be the root cause of therapeutic resistance, recurrence, and tumor progression. CSCs are considered to be modulated by overexpression of certain pathways, including signal transducer and activator of transcription 3 (STAT3). The aberrant activity of STAT3 has been identified in clinical inspection of > 70% of breast and prostate cancer and its inhibition by various mechanisms holds unprecedented significance in modern medicine. Niclosamide (Nic), an FDA approved anthelmintic drug, has recently been reported as potent inhibitor of STAT3 and it is seen to trigger the activation of cancer cell apoptotic mechanism. Despite its promising cancer treatment capabilities, lack of solubility is a major bottleneck limiting its bio-availability. To circumvent the issue, we adopted a nanomedicine approach integrated with a surface decorated cucurbituril (CB[6]) host-guest chemistry using luminescent carbon nanoparticles (Nano-Carbobitaceae) for sustained and enhanced delivery of niclosamide traceable with vibrational spectroscopic methods. Carbon nanoparticles (Hydrodynamic dynamic size=55±1 nm) were obtained *via* the environmentally benign hydrothermal synthetic route using food grade Agave nectar as the carbohydrate source. The particles were either prefunctionalized (hydrodynamic dynamic size= 76±13 nm) or postfunctionalized (hydrodynamic dynamic size= 93±4 nm) with CB[6] and were further loaded with STAT3 inhibitor Nic. Extensive physiochemical characterizations were subsequently carried out to confirm the binding of Nic and CB. FTIR results indicated a 2:3

complexation model. Furthermore, the ^{1}H NMR results showed shifts in the characteristic peaks of Nic upon encapsulation in CB[6] cavity.

The potential of the developed particle for the *in vitro* applications was evaluated. Interestingly, the hydrodynamic size of the particles was mostly preserved in various physiologically relevant media. Approximately two- fold enhancement in IC_{50} values were observed for the encapsulated drug versus free drug. The IC_{50} value of Nic, CB[6] Nic and CB[6] CNP Nic (post functionalized) was determined to be $(45\pm04)\times10^{-6}$ M, $(28\pm03)\times10^{-6}$ M and $(21\pm02)\times10^{-6}$ M, respectively. Our results indicated that this novel nanoplatform holds promise for sustained and enhanced chemotherapeutic delivery of sparingly soluble Nic for modulation of stem cell signaling pathways.

ACKNOWLEDGMENT

First and foremost, I would like to express my sincere gratitude to my advisor Professor Dipanjan Pan for his excellent guidance, caring and encouragement. I am grateful to him for his infinite patience to answer my endless questions and helping me to find my feet both in my research and my life. I would like to appreciate the assistance of the entire MatMed lab. Special thanks go to my mentor and coauthor Dr. Santosh Kumar Misra and our collaborator Dr. Prabuddha Mukherjee for their insightful discussion and great assistance in carrying out the experiments. Thanks to Ayako Ohoka, Harris Nisar and Zach Saldivar. I would also like to express my gratitude to Materials Research Lab staffs, Roger Adams NMR Lab director (Dr. Dean Olson), Illinois sustainability center (Mr. John Scott), Rodríguez-López Lab members (Mr. Mark Burgess and Mr. Burt Simpson), Mr. Julio Francisco Serrano and Mr. Long Luu for assisting me in carrying out some of the experiments.

Words cannot describe my gratitude and respect to my parents as my first teachers in my life. Despite being physically distant, I will never forget all the unconditional support you provided for me to make me what I am today. I deeply missed you both. I would like to appreciate the mental and academic support from my brother.

This work was financially supported by funds from University of Illinois at Urbana-Champaign and Children's Discovery Institute.

Table of Contents

LIST OF FIGURES

LIST OF TABLES

CHAPTER 1

INTRODUCTION

1.1 CANCER STEM CELL THEORY

Cancer poses a death toll of ~8.2 million people every year. In the United States alone a total of 1,658,370 new cancer cases and 589,430 cancer deaths are predicted to occur in 2015. Although cancer is currently the second most vicious disease after cardiovascular disease in the US, it is envisioned that the death burden would soon surpass that of heart disease in coming years [1]. Common methods of therapy such as primary tumor excision, chemotherapy and radiotherapy are usually partially successful in reviving the patient as there is a high probability of tumor relapse. The conventional therapy only preferentially abolishes differentiated cells whilst leaving behind small self- renewing, tumorigenic population of cells called "cancer stem cells" (CSCs) which show resistance to treatment [2].

The emerging theory of CSCs came into vogue after the pioneering work of Dick and colleagues in the context of hematological malignancies [3, 4]. The model postulates that tumors are arranged in cellular hierarchy of heterogeneous cell populations with various molecular profiles as a result of the presence of small sub population of malignant cells coined as "cancer stem cells" (CSC) or "tumor initiating cells" (TICs) [5, 6]. The inherent phenotype of this subpopulation is that they share common attributes of normal tissue stem cells and they are capable of renewing themselves *via* symmetric or asymmetric cell division and also indefinitely differentiate to give rise to malignant tumors [7]. They are also known to exhibit plasticity in that

they reversibly switch between the stem and non- stem cell characteristics [8]. CSCs have been reported to be invariably occur in various human solid tumors namely, breast [9], colon [10] and brain [11].

The hallmark quality of CSC is the expression of specific surface markers. For instance, in the case of breast cancer initiating cells, four surface antigen profile namely CD44, CD24 (adhesion molecules), B38.1 (breast/ ovarian cancer specific marker) and ESA (epithelial specific antigen) have initially been identified by Al- Hajj *et al*. as the main biomarkers of the CSCs [9]. The contribution from these factors was such that all the immunodeficient mice with $CD44^{+}$, $B38.1^{+}$ or $CD24^{-}$/low injection established palpable tumors in twelve weeks which was contrasting the $CD44^{-}$, $B38.1^{-}$, or $CD24^{+}$ injection receiving mice. Table 1.1 summarizes the main biomarkers in distinguishing the CSC population. In addition to the aforementioned screening method, other methods such as flow cytometric evaluation of side population cells based on reduced uptake of Hoechst 33342 DNA binding dye [12] and aldefluor™ assay [13] hold prominence.

As opposed to the former theory, another parallel model under the title of "clonal evolution model" exists. It follows the same principle as the Darwinian approach towards evolution and it states cancer progression is the consequence of the selection of the fittest variant. All of the differentiated cells in the clone have the capability of acquiring sufficient bias on the DNA sequence level so as to mutate and become metastatic while others become quiescent [14-16]. The authenticity of both hypotheses is highly debatable and it is not clear which model has more robust ground in describing the aggressive behavior of cancer. Figure 1.1 compares and contrasts the two proposed models of tumor growth.

Table 1.1 Biomarkers in the detection of cancer stem cell subpopulation. Reproduced with permission from Ref. [17]

Marker	Description	Marker	Description
CD24	Heat Stable Antigen, luminal	CD31	Endothelial marker
CD29	Beta 1 integrin	Ter119	Hematopoietic marker
CD44	Hyaluronic acid receptor	CD140a	Stromal marker
CD49f	Alpha 6 integrin	CD133	Prominin-1
CD326	Epithelial surface antigen (ESA), EpCam	CD201	PROCR, protein C receptor
CD45	Hematopoietic marker	CD166	Activated leukocyte cell adhesion molecule (ALCAM)

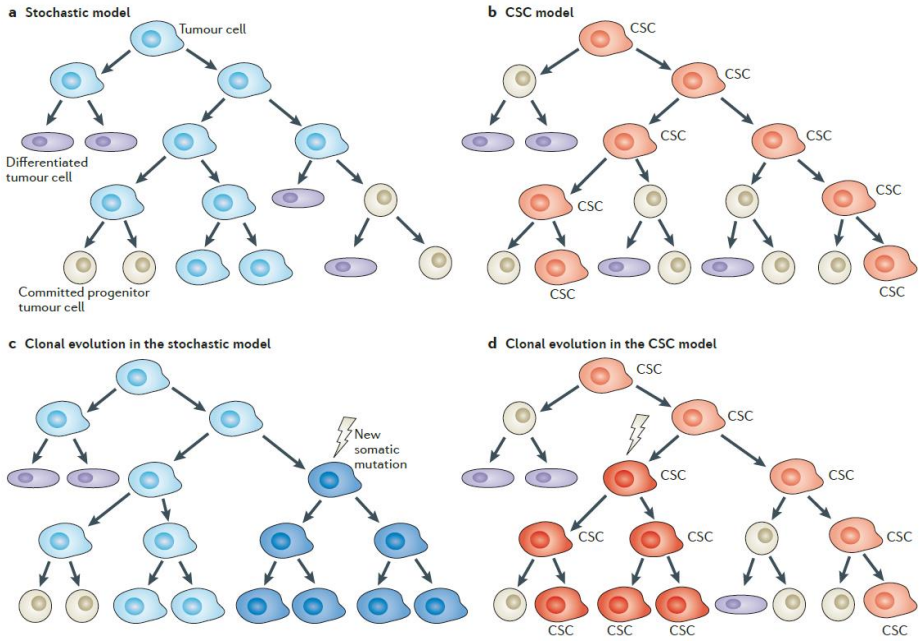

Figure 1. 1 Various models of tumor growth. Reproduced with the permission from Ref. [18].

CSCs are resisting towards anti neoplastic therapy through various defense routes which can be narrowed down into two major groups: CSC- intrinsic and CSC- extrinsic [19]. The former is attributed to the DNA repair pathways [20], drug pump expression [21] and cell cycle alteration [19] while the latter is mostly concerned with the role of tumor microenvironment [22]. Similar to the normal stem cells, CSCs are thought to be residing in a microenvironment known as CSC niche which mediates the stemness, proliferation and immortality of stem cells [23]. Niche is distinguishable in their microenvironment in terms of anatomy which consists of fibroblasts cells, endothelial cells, immune cells and growth factors. CSC niche, on the other hand, accompanies the non- malignant cell population as well as pathogenic cells which release factors contributing to the angiogenesis and the promotion of tumor cell metastasis [24-26]. Additionally, the niche also has the responsibility to protect the cells from the invasion of genotoxic agents, a factor that justifies the CSC resistance towards therapy [23]. Not only does CSC niche sustain the immortality and self- renewal of these subsets but it also elicits them with the capability to induce epithelial-mesenchymal transition (EMT), a process known to be involved in tumor progression [27]. There is a well-established link between EMT and the abundance of inflammatory cues (e.g. IL-6, IL-8, TGF-b1, NF-κB, TNFa and HIF-1) in the CSC microenvironment. The activation of inflammatory molecules, in turn, results in the activation of downstream self- renewal pathways such as JAK/STAT, NOTCH, MAP-Kinase/ERK, the PI3K/AKT, NF-κB, Wnt and TGFβ which regulate CSCs [28]. Therefore, over the past years there has been a paradigm shift towards the novel cancer treatment methods that specifically target the aforementioned pathways to fully combat cancer.

1.2 ROLE OF JANUS-KINASE (JAK)/ SIGNAL TRANSDUCER AND ACTIVATOR OF TRANSCRIPTION (STAT) PATHWAY IN TUMORIGENESIS

As already mentioned, one of the common cytokine signaling pathway is Janus-Kinase (JAK)/ Signal Transducer and Activator of Transcription (STAT) pathway which was discovered in the context of interferon-α (IFNα)-, IFNγ- and intereukin-6 (IL-6)- mediated downstream signaling [29]. STAT family which consists of seven members (i.e. STAT1, 2, 3, 4, 5a, 5b and 6) are the latent cytoplasmic proteins which function as signal messengers and transcription factors. Besides, they contribute to the normal cell responses to the cytokines and growth factors [30]. STATs are involved in numerous physiological activities due to regulation of many genes including the genes involved in cell cycle progression, cell survival, differentiation, metastasis, apoptosis, angiogenesis and immune responses [31]. STAT activation begins with the dimerization of cell surface receptors upon the attachment of cytokines which leads to the activation of JAK tyrosine kinases. In the next step, the docking sites for the SH_2- domains which are dominant in all STATs are created due to the phosphorylation of the residual tyrosine on the receptor. Subsequently, the receptor- bound STAT is phosphorylated by JAKs and translocate to the nucleus where they activate the transcription regulation of variety of genes. Another suggested mechanism is the activation of STATs in response to growth factors such as epidermal and platelet- derived, hepatocyte growth factors [32-34]. The signaling cascade is demonstrated in Figure 1.2.

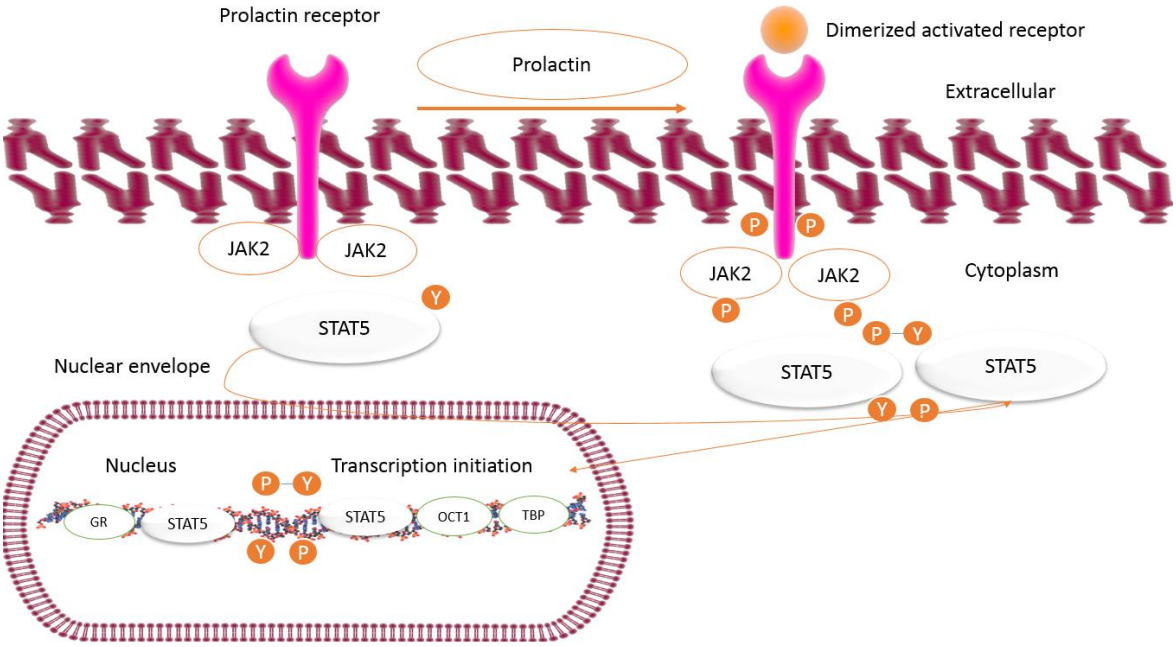

Figure 1. 2 JAK/STAT signaling pathway.

Of particular interest in the STAT protein family are the STAT3 and STAT5 whose role are prominent in cancer progression [35]. Considering the precise function of STAT3 in regulating cell functions, its aberrant activity would lead to devastating consequences; their pivotal role in transducing signal from several receptor and non- receptor tyrosine kinases activated in cancer cells has already been identified [36]. The first evidence highlighting the role of STAT3 activation in cancer cell was demonstrated in multiple myeloma where the apoptosis was effectively suppressed as a result of anti- apoptotic proteins Bcl-xL [37]. Later, it was discovered that STAT3 is constantly regulating the essential proteins for cancer cell sustention such as c-Myc [38], Cylin D1 [39] and Survivin [40] in human cancer cells. Subsequently, the activation of STAT3 protein has been observed in several cancers such as breast [41], lung [42], colorectal [43], esophageal [44], bladder [45, 46] and prostate [47]. Intriguingly, clinical data shows that STAT3 is persistently active in greater than 70% of prostate and breast cancer cells

[48]. More recently, the role of STAT3 has been linked to the CSC expansion and maintenance. Examples include the cooperation of STA3 in breast CSC [49], liver cancer [50], glioblastoma [51] and bone sarcomas [52].

Considering the high correlation level between aberrant activity of STAT3 and human tumors prognosis, it is promising to engineer therapeutic approaches that specifically inhibit this particular pathway in combating cancer. Therefore, strategies have been developed to inhibit these pathways each of which functioning at a particular level, including the tyrosine-phosphorylation step for the activation of STAT3, DNA binding, association with other transcriptional co- activator, RNA inhibition and modulation of upstream regulators [53, 54]. Due to the extensive redundancy among cytokines, the most effective method is considered to be directly targeting STAT3 protein through NH_2- terminal, DNA binding, and SH_2 domains [55]. For instance, SH_2 domain is considered as an appropriate target for blocking the STAT3 dimerization by peptides, peptidomimetics and small molecule inhibitors [54]. Other chemical includes natural compounds and their derivatives namely curcumin, curcubitacins, indirubin and platinum complexes [55]. Recently, niclosamide has been regarded a drug for effectively suppressing the activity of this pathway [56].

1.3 TARGETING STAT3 PATHWAY: NICLOSAMIDE

Niclosamide (Nic) with the systemic name of (5-chloro-N-2-chloro-4-nitrophenyl)-2 hydroxybenzamide ($C_{13}H_8Cl_2N_2O_4$, MW: 327.119) (Figure 1.3), is an FDA approved small-molecule anti- helminthic drug for the treatment of human gastrointestinal tapeworm *via* oral administration and has been in market for approximately 50 years [57, 58].

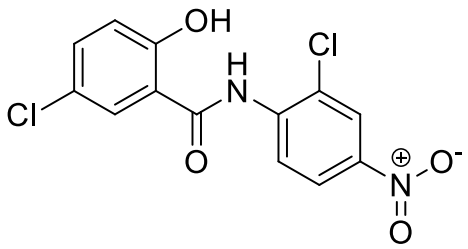

Figure 1. 3 Molecular structure of niclosamide.

It has been suggested that Nic's anthelminthic effects are exerted through the inhibition of oxidative phosphorylation leading to the stimulation of adenosine triphosphatase in the mitochondria of tapeworm. This process subsequently debilitates the scolex and proximal segments of tapeworm both *in vivo* and *in vitro* [59]. Niclosamide has also been successfully applied as molluscicide for water treatment in schistosomiasis control program and has effectively functioned against severe acute respiratory syndrome (SARS) virus [60, 61]. Over the last five years, researchers have acknowledged the anti- neoplastic properties of the drug and its potential application in effective treatment of cancer [56]. The motivation behind the development of cancer drug based on a non-cancer drug originates from the fact that many diseases share common molecular and cellular pathways [62]. The superiority of the repositioning of an already FDA- approved drug is that it drastically reduces the cost burden of inventing new formulation considering that the drug development requires an average of 11 years of research and investment of US $1.8 billion to translate the new agent from bench to bedside [62]. Generally, for a drug to receive FDA approval, the drug has to pass phase III clinical trial stage in addition to extensive research on cell and animal models [63]. Moreover, the existing drug has well- defined pharmacokinetics and safety profile in human application for decades. As a result of this, a preclinical and phase I study proposed in this work is highly appropriate. With a successful outcome, the drug can be swiftly translated to phase II and III

clinical studies [64]. Interestingly enough, Nic exhibits the inhibitory effects towards the pathways modulated in CSCs namely, Wnt/β-catenin [65, 66], mTORC1 [67], STAT3 [56, 68, 69], NF-κB [70] and Notch [71]. For instance, Wang et al. [72] utilized high throughput drug screening methods to investigate the effect of candidate formulation on the extracted stem like side population (SP) breast cancer both *in vivo* and *in vitro*. In this research, niclosamide was rendered to down regulate the stem pathways such as Wnt/β-catenin, Notch, Hedgehog and induced apoptosis in the breast cancer cells. Furthermore, *in vivo* studies corroborated the therapeutic efficiency of the drug. In the same vein, out of the 1,200 clinically available formulations tested for the inhibition of stem like ovarian tumor- initiating cells (OTIC), Nic constitutively exhibited superior selectively towards CSC subpopulation both *in vivo* and *in vitro* [73]. The authors claimed that Nic is perturbing the metabolic pathway essential for biogenesis and redox regulation. Specifically, the potent inhibitory effects of Nic towards the STAT3 pathway are attributed to the disruption of transcriptional activities due to phosphorylation abrogation and nuclear translocation of STAT3. Inhibition of STAT3- mediated stem cell marker OCT-4 through the application of Nic has been achieved by Kim et al. in MDA- MB-231 cells [74]. Furthermore, through a synergistic approach, Nic inhibited STAT3 phosphorylation and resulted in sensitization of human head and neck cancer cells to Erlotinib treatment [75]. This combinatorial approach effectively suppressed the epidermal growth factor receptor highly overexpressed in the human head and neck.

Despite the promising cancer treatment capabilities, lack of aqueous solubility is a major drawback limiting the bio-availability of Nic. It is reported that the oral bioavailability of Nic in Sprague-Dawley rats is only 10% [76]. In fact, the drug is virtually insoluble in water with a solubility window of 5-8 mg/l at 20 ºC yet its solubility increases upon the pH increase. Several

strategies have been employed in order to combat this obstacle; amongst which are the encapsulation of the drug in the PAMAM dendrimers and cyclodextrins (HP-β-CD, β-CD) [77], preparation of solid dispersion with PEG6000 [78], synthesis of a water soluble analog – phosphate of niclosamide (p- niclosamide) [70] and very recently the use of rigid core micelles as an effective nanoscale strategy by our group [79]. While these approaches indeed offered some advantages, their potential for clinical translation has not fully been realized yet.

1.4 SUPRAMOLECULAR CHEMISTRY

Supramolecular chemistry or the "chemistry beyond the molecule" examines the interaction between several molecules and the induced properties as a result of that interaction. The interests on the structure and amazing abilities of enzyme was the cornerstone for the introduction of this relatively new field [80]. The field gained such a huge popularity that in 1987 the Nobel Prize in chemistry was endowed to Lehn, Pederson and Cram "for syntheses of molecules that mimic important biological processes". The dynamic realm of supramolecular chemistry encompasses host-guest chemistry, molecular self-assembly, mechanically-interlocked molecular architectures and dynamic covalent chemistry [81].

The forces in the supramolecular chemistry are of paramount importance and are non-covalent in nature. The non- covalent forces can further be classified into electrostatic interaction (i.e. ion- ion, dipole- dipole and ion- dipole interactions), hydrogen bonding, π- interactions (π-π stacking, anion- and cation - π interactions), van der Waals bonding and hydrophobic effects). A myriad of research interests have been attracted towards the host- guest chemistry which involved a binding phenomenon between a large molecule, coined as host, and a small molecule

called guest.The host molecule is in the form of cavitand[1] allowing the reception of a guest molecule. The common host molecules are cyclodextrins [82], calixarenes [83], pillararenes [84], cucurbiturils [85], metallacrowns [86], crown ethers [87] and cryptophanes [88]. The structure of some of the host molecules are demonstrated in Figure 1.4.

The implication of the weak association of host and guest molecule, due to the inherent nature of non-covalent interaction, is the reversible binding of the reaction constituents. This extraordinary property has been extensively exploited in molecular switches [89, 90], drug delivery [91, 92], catalysis [93, 94], dye tuning [95, 96] and in enzyme interaction [97, 98].

A key feature of the host is its tendency to accommodate specific guest molecules with complementary properties (size, binding type, size, etc.) due to conformation constraints which is known as selectivity. Upon the introduction of an external stimulus, the structure can reorganize itself towards more thermodynamically stable state. This capability is utilized in stimuli-responsive functional materials.

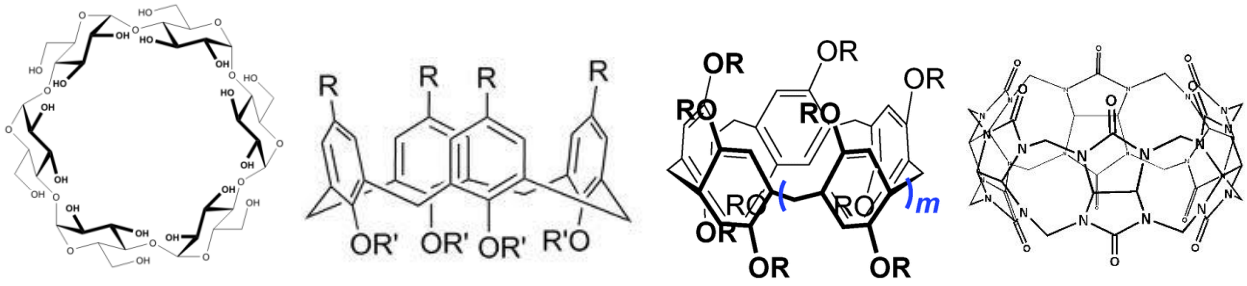

Figure 1. 4 The structure of some common guests: a) α cyclodextrin, b) calix[4]arene, c) pillararenes d) cucurbiturils.

[1] Container shaped molecule

1.5 CUCURBITURILS

Cucurbit[*n*]urils (CB[n]) are a family of cyclic oligomers resembling *Cucurbitaceae* (the Latin word for pumpkin). Although CBs were initially derived in 1905 through the condensation of glycoluril and formaldehyde under acidic conditions, its chemical structure remained largely unknown until 1981 when Mock and coworkers characterized the structure by NMR and IR spectroscopy [99]. It was revealed that the structure consists of macrocyclic hexamer glycoluril joined together with methylene bridges (CB[6]) [99]. Afterwards, other homologues of CB were introduced and the family expanded to include CB[5], CB[7], CB[8] and CB[10]. CB are barrel-like structures with two hydrophilic portals lined ureido carbonyl rims and a hydrophobic cavity which enable the encapsulation of neutral molecules and positively charged species through ion-dipole interaction. In addition, another mode of interaction is the hydrogen bonding between protonated molecules and negatively charged carbonyl ring. The cavity depth of CBs is 0.91 nm and the cavity sizes of CB[6], CB[7], and CB[8] correspond to α-, β-, and γ-CD, respectively where the sizes are provided in Table 1.2 [100]. While the overall properties of CBs are closely analogous to those of calixarenes and cyclodextrins, the presence of two linkers holding subunits together imparts it with improved structural rigidity, high degree of preorganization and superior binding selectivity. Extremely high binding affinities as high as 7.2×10^{17} M^{-1} has been reported for CB guest complex which is comparable to avidin-biotin pairs [101]. The comparison of the properties of different homologues of CB has been summarized in Table 1.2.

Supramolecular host molecules such as cyclodextrins are orally and topically administered in clinical settings for drug delivery purposes. If cyclodextrins enter body in the non metabolized state they would be nephrotoxic. The poor selectivity of CD leads to usage of higher doses of cyclodextrin- containing formulations and boosts the chance for leaving CD

unmetabolized resulting in nephrogenic symptoms [102]. Nevertheless, the unique merits of CB have made it a promising unrivaled candidate for next generation targeted drug delivery systems. Amongst its various desirable properties, one can allude to the cytotoxic safety of CB, rendering its potential for biological- based purposes [103]. For instance, (4,5-dimethylthiazol-2-yl)-2,5-diphenyltetrazolium bromide (MTT) colorimetric cell viability assay in Chinese Hamster Ovary cells (CHO-K1) revealed no cytotoxicity at dosage up to 1 mM (IC_{50}=0.53 mM) after 48 h of incubation [104]. Furthermore, no appreciable internal damage to the cell membrane was observable in fluorescent assessment of CB internalization, implying the appropriateness of CB for *in vitro* and *in vivo* applications. Intravenous administration of CB further corroborated that CB is well- tolerated (up to 200 $mg.kg^{-1}$) and induces no acute toxicity in mice. In another study, the cytotoxicity, uptake and bioavailability of CB and its derivate have been investigated. High cell tolerance (up to 1 mM) and efficient cellular uptake was reported [105].

One of the biggest challenges with hydrophobic drugs is their poor aqueous solubility leading to low bioavailability. In fact more than half of the newly developed chemical drugs suffer from low solubility despite showing promise in cancer therapy, hence hindering their applications [106, 107]. Interestingly enough, host-induced guest solubilization can mitigate this obstacle where the enhanced effect is mostly appreciable in drug delivery to bodily fluids rich in salt and acid [92]. For instance, it has been shown that benzimidazole- based drugs show enhanced bioavailability in the presence of CB[7] which is due to the "host- induced guest protonation" [108]. The drug possesses significant solubility in protonated state. Through binding with CB[7], the pKa values of the conjugate acid is enhanced by 2-4 units which implies the stabilization of the protonated form of the drug, thus increasing solubility. Similarly the solubility of camptothecin (CPT), an FDA approved DNA enzyme topoisomerase I (topo I)

inhibitor, was enhanced up to 0.4 and 47 μM in the presence of CB[7] and CB[8], respectively [109]. Furthermore, the photostabilization of the drug has also been reported as a result of CB encapsulation [108]. CB also assisted in maintaining the amorphous structure of the drug while preventing polymorph interconversion [110]. Perhaps the most distinctive feature of CB in drug delivery is drug stabilization owning to the shielding effects towards the guest which makes the formulation less prone to nucleophilic attacks in the bulk of the solution. Specifically, extensive research has been carried out on platinum- based anti- neoplastic agents [111-113]. The issue with the platinum (Pt)- based drugs is the high reactivity of chloride, carboxylate and ammine ligands in the formulation towards peptides and plasma proteins with thiol functionalities which will lead to drug inactivation. It was realized that the encapsulation of the drug by CB can block the nucleophilic attack by exerting steric hindrance [111]. In addition, due to the binding of CB to the hydrophobic part of the ligands, the platinum metal is placed near the portals of CB thus further helping the protection [103]. Later cisplatin was taken to demonstrate the effect of CB on the potency of the drug [111]. The *in vitro* cytotoxicity indicated no significant difference between the free drug and CB- encapsulated drug on the human ovarian carcinoma cell line A2780 and its cisplatin- resistant subunit A270/cp70 tumors and MCP1. Intriguingly though, the *in vivo* results from CB-cisplatin complex showed significant enhancement in suppressing the tumor growth compared to cisplatin on human tumor xenograft. The authors simply attributed the observation to the pharmacokinetic effects where CB promotes the total circulating cisplatin over the period of 24 h and suppresses drug resistance. In conclusion, CB is highly regarded as a promising drug carrier considering all its properties combined.

Table 1. 2 General structural parameters and properties of Cucurbit[n]uril family (Average dimensions are determined from the crystal structure with the CCDC code COQWOV [114])

Macrocyclic molecule	Internal diameter (nm)	External diameter (nm)	Height (nm)	Calculated volume (nm^3)	Solubility in aqueous solution	Binding selectivity towards
CB[5]	0.44	0.24	0.91	0.068	20-30	alkali metals, ammonium, some transition metals, neutral gas molecules
CB[6]	0.58	0.39	0.91	0.142	<0.01	most metals, including alkali, alkali earth, and some transition metals, aliphatic guests e.g. ammonium and diammonium cations, amines, polypeptides, and
CB[7]	0.73	0.54	0.91	0.242	20-30	most aliphatic and aromatic compounds, ferrocenes, adamantanes, and metal
CB[8]	0.88	0.69	0.91	0.367	<0.01	Same as CB[7], larger guests that CB[7] cannot bind to such as fullerenes, can form 1:2 complexes
CB[10]	1.00	2.00	0.91	0.691	0.05	Smaller hosts such as CB[5] and modified calix[4]arene

1.6 CARBON NANOSPHERES

Since the introduction of fullerene, other classes of carbon nanomaterials such as carbon nanotubes (CNTs) [115], graphene [116], nanodiamonds [117], carbon dots [118] and very recently nanothread [119], have generated a plethora of research interest amongst scientists due to their favorable properties that make them suitable for applications in composites, electronics, photonics and biomedicine. Of particular interest in this expanding family is the fascinating class of carbonaceous nanomaterials denoted as carbon nanodots also known as carbon quantum dots or simply carbon dots (CDs). It is important to demarcate the difference between carbon dots and graphene dots despite their similarity in chemical and physical properties in many aspects. The difference, though, stems from their size and their synthetic routes, where graphene dots have lateral sizes up to 100 nm and are commonly obtained from graphene based precursor whereas CDs refer to particles with aspect ratio of 1 and below 10 nm in diameter [120]. In 2004, fluorescent CDs were discovered by serendipity through the process of purifying single walled carbon nanotubes (SWCNT) *via* arch discharge method [121]. The abundance of surface functional groups such as carbonyl, carboxyl, epoxy, amino, and hydroxyl endow CDs with high aqueous solubility [118]. Moreover, their nearly spherical shape, simplicity of surface functionalization and facile synthetic routes are amongst the attributes that offer superiority over the rest of the carbon nanomaterials family. In general, the synthetic routes of CD can be divided into bottom-up and top-down approaches and include methods such as laser ablation [122], microwave pyrolysis [123], hydrothermal treatment [124] and electrochemical reduction [125]. Versatile precursors have been tried for the synthesis of the CDs such as glucose [126], glycerol [127], candle soot [127], orange juice [128], banana juice [129], tea [130], caramel [131] or in

Nescafe®coffee [132], molasses [133] and honey [134] indicating the ease of production and the potential of scale- up fabrication of these nanoparticles.

In the past few years, extensive research has been directed to exploit the luminescence properties of CDs which is urged by the demands in the progressive field of optical imaging. These particles are overtaking semiconductor quantum dots by virtue of excellent biocompatibility as opposed to the potential cytotoxicity of QDs due to the presence of heavy metals [135]. In addition, they surpass organic dyes in photostability and high quantum yield as well as not indicating photobleaching and blinking [136]. The fluorescent properties of CDs are mainly dependent on the synthetic method and the type of surface passivation. Extensive research has been conducted to demonstrate the mechanism of fluorescence in CDs; although there are still large controversies regarding the origin of the phenomenon. The two predominant proposed mechanisms include the radiative recombination of surface confined electrons and holes leading to the creation of excitons and quantum confinement of emissive deep energy traps which become more emissive upon the astute choice of surface passivation method [137]. Despite the lack of knowledge about the radiation mechanism, CDs have already been exploited for *in vitro* and *in vivo* fluorescent imaging [138], Raman imaging [139], photoacoustic imaging [140] and photosensitizing for photodynamic therapy [141]. For instance, Sun's group reported on the potential of CD in two- photon luminescence microscopy in MCF-7 (human breast cancer) cell line [142]. Furthermore, HepG-2 (human liver carcinoma) cells have been incubated with CDs and subsequently were imaged. Cell internalization of CDs was observed by confocal microscopy or even common fluorescence microscopy. Hsu et al. [143], used LLC-PK1 (pig kidney cell line) to elucidate the applicability of CDs for cell imaging. It was plausible that cells internalized CDs by endocytosis pathway. Upon excitation at long wavelength, red fluorescence

signal was detectable. The photostability of CD was demonstrated to be remarkably high without exerting prominent cytotoxic effects.

Photoacoustic (PA) imaging, as a hybrid imaging modality, enjoys the merits of both optical and ultrasound imaging for deep tissue penetration as well as high spatial resolution [144]. An ideal contrast agent for PA imaging should meet some criteria such as high photon absorbance and efficient ability to convert light to heat [137]. In this regard, our group did a pioneering research on CD applications [140]. Specifically, they exploited the honey derived CD as contrast agent for PA imaging of sentinel lymph node to monitor the cancer staging in a real-time manner. The CD had reasonable lymphatic transport rate and also contributed to >9 fold enhancement in the PA signal over the rat's blood suggesting the potential of CDs as contrast agents for PA imaging during intraoperative SLN biopsy intervention. Overall, these studies corroborated the promise of CD as efficient optical nanoprobes.

1.7 EVALUATION OF THE CYTOTOXICITY OF CARBON NANOSPHERES

Thorough studies on the toxicity of CDs are desired before their translation into the clinic. Based on the current assessment of the data in literature, it is quite established that CDs are generally nontoxic and in some studies it was shown that the surface passivizing polymer worsened its toxicity profile [145, 146].

As already disucssed, CDs surpass their QD counterparts in biocompatibility. In a recent study, the relative toxicity of three pristine nanomaterials were examined [147]. It was realized that toxicity of QDs>>Au nanoparticles>C-dots with IC_{50} values for normal NIH/3T3 (Mouse embryonic fibroblast) cells as 0.98, 62, and 250 $\mu g.ml^{-1}$, respectively.

MTT and Trypan blue assay were utilized on HepG2 cells to evaluate the cytotoxic effect of CDs during 24 h incubation [148]. The cell viability upon exposure to 0.5 mg. ml^{-1} ranged between 90-100%. The concentration was increased to values as high as 10^2 and 10^3 times more than the dose required for bioimaging, suggesting the minimal toxicity for bioimaging. In addition, Sun et al., explored the *in* vitro and *in vivo* cytotoxicity of CDs [149]. MTT results revealed >80% cell viability for CD in MCF-7 for concentration of 0.1 $mg.ml^{-1}$. The *in vivo* results using CD-1 mice demonstrated that after 4 weeks of intravenous administration of CDs, no mice suffered from adverse clinical signs including anorexia, hair loss, scab, vomiting, or diarrhea. The bodies' normal functions were not impaired compared to control group and was maintained at similar level irrespective of the dosage and time indicating no cytotoxicity. Although analysis of harvested tissue showed the presence of CDs in liver, spleen and kidneys, the level of accumulation was minor. Furthermore, Yang et al. [149] conducted a study on CD-1 mice for over 90 days. No mortality, lesion, or considerable weight change was observed at the dosage of 20 $mg.kg^{-1}$. In a more recent study, athymic nude mice bearing subcutaneous SCC7 tumors, were exposed to CDs conjugated to NIR dye to track the fate of the CDs *in vivo* [150]. The nanoparticles were administered *via* three routes namely, intravenous (IV), subcutaneous (SC), and intramuscular (IM). All three routes were appropriate for the clearance of CDs, with IV being the fastest pathway. The system underwent rapid clearance, yet passive tumor targeting. The prime clearance route was through the kidney. Besides, reticuloendothelial system (RES) evaluation indicated the minimal uptake of particles by this route and rendered improved tumor to background ratio. Furthermore, tumor accumulation was higher in SC and IV injection than IM injection. In a nutshell, the toxicity of CD can be considered very low and cytotoxicity, if

any, would be exerted through surface functionalization which can be reduced by the appropriate choice of passivation agent.

1.8 CARBON NANOSPHERES IN DRUG AND GENE DELIVERY

CDs can also serve as a platform for controlled drug and gene delivery due to their high surface to area ratio, excellent biocompatibility, small size for being taken up by solid tumors and most importantly, being rich in surface functional moieties appropriate for the incorporation of various compounds for targeting strategies. These features combined with their bioimaging potentials have turned them into promising "theranostic" candidates. For instance, Zhou et al. [151], came up with a pH- responsive nanocomposites of CDs and mesoporous silica for drug delivery and optical imaging purposes. The Dox loaded CD gated nanocarrier exhibited enhanced efficacy in treating cancer cells as the cargo was efficiently taken up by the cancer cells through endocytosis pathway as has been confirmed by fluorescent microscopy. Moreover, the nanocomposite acted as non- invasive vehicle for *in vitro* and *in vivo* tracking of the therapeutic agent. Zheng et al. [152] reported on the multifunctional theranostic agent with the conjugation of a variant of anti-cancer drug oxaliplatin (Oxa) on the surface of CDs. The formulation of Oxa was changed such that it incorporated carboxyl groups to react with amino functionalities of CDs. MTT assessment of the nanoformulation on HepG2 cells revealed the IC_{50}= 3.4 $\mu g.ml^{-1}$. The nanocarrier manifests the ability in eradicating 82.4% of tumor size after three days *in vivo* after two doses of CD-Oxa (0.72 $mg.ml^{-1}$ of Pt, 20 μl) in Chinese Kun Ming (KM) mice injected with hepatocarcinoma 22 cell line (H22) liver cancer. In addition, during the course of treatment the drug can be traced due to fluorescent properties of CDs which helps customize the injection time and dosage of medication. Very recently, our group has reported on the application of luminescent carbon dots (LCN) for synchronized imaging and delivery of pentoxifylline (PTX), an anti-inflammatory

drug which has been repurposed for targeting melanoma [139]. The surface tuning of the particles was achieved either by PNIPAM polymer which was labeled as temperature responsive (TR-LCN) set or multiarm polyethylene glycol (MA-PEG) called MA-PEG-LCN. Two nanoparticle surface coatings were compared with each other in terms of therapeutic efficacy and release pattern. Thanks to the choice of coating, LCN could emit in NIR region which is the relevant imaging window for deep tissue penetration and prevention of autofluorescence from organs. After rigorous physiochemical characterization of the nanoformulations, the *in vitro* release behavior was inspected. The two delivery systems contrasted in drug release behavior in that the MA-PEG-LCN exhibited higher loading efficiency compared to TR-LCN. Moreover, the total drug release in MA-PEG-LCN particle was lower compared with TR-LCN. It was also realized that TR-LCN exhibited burst release at room temperature as opposed to gradual release at 37 ºC. The authors conjectured that the former can be utilized for immediate therapy purposes. Subsequently, incubation of C32 melanoma cells with MA-PEG-LCNs and TR-LCN was executed and the cells were observed using infrared and Raman imaging where it was shown that the two formulations treated their cargo differently. Although MA-PEG-LCN indicated ydistribution all over the cells, TR-LCNs adopted more selective localization. No significant difference was conceivable in the imaging ability of TR-LCNs and MA-PEG-LCNs, although the stimuli- responsiveness of TR-LCNs can be exploited for therapeutic and imaging purposes simultaneously. The author further utilized the unique properties of CDs for *ex vivo* fluorescence, NIR and Raman imaging on the pigskin. They could successfully image the TR-LCNs particles incubated in the pig skin where they observed homogenous destruction of the particles in the samples. Furthermore, as a proof of concept to show deep skin imaging in NIR region, pig skin treated with MA-PEG-LCNs were employed and they could localize signal at approximately 100

μm from the surface. Although similar experiment for TR-LCNs treated skin was impeded due to fluorescence quenching from the particles, it was concluded that the particles hold promise for further investigation in NIR imaging *in vivo*. Table 1.3 summarizes some of the researches executed using CDs as drug delivery, gene delivery or theranostic agent.

Table 1. 3 Recent advances in the application of carbon dots for theranostic applications.

Reference	Agent Application and Prominent Results
Misra et al. [153]	CDs-DNA complex (CNPLexe) was efficiently transfecting green fluorescent protein reporter gene containing pDNA. Higher cell viability of polyethylenimine (PEI) coated CDs compared with PEI was noticed.
Hu et al. [154]	Branched polyethyleneimine-based carbon dots (PCD) are prepared from branched polyethyleneimine. The particles show potential for gene delivery and bioimaging as has been confirmed by gene transfection studies.
Wang et al. [155]	Hollow CDs were prepared from bovine serum albumin (BSA). Particles were ca. 6.8 nm in size with 2 nm pore size. DOX was loaded and its release showed pH triggered manner. The immediate uptake of the system was observed by bioimaging indicating their potential in biolabeling and cell tracking.
Pandey et al. [156]	CD on the surface of Gold nanorod (GNR) was employed for delivery of DOX. It was envisioned that the particles be applicable in drug delivery, photothermal therapy and biological imaging.
Tang et al. [157]	Direct and sensitive Förster resonance energy transfer (FRET)-based CD drug delivery system was reported to do real time monitoring of pH- mediated DOX release. CD dot was used as platform for drug delivery and as donor of FRET pair to be highly sensitive on the separation distance. Furthermore, two photon imaging of the system at tumor tissue level was tested.
Chen et al. [141]	Photodynamic therapy drug, Chlorin E6 (Ce6) was conjugated to CD for photodynamic therapy (PDT) and photosynthesizer fluorescent detection (PFD) of gastric cancer *in vivo*. It was demonstrated that the theranostic platform was successful for NIR imaging and represented good tumor- homing ability.
Kim et al. [158]	Fluorescent CD-PEI/Au-PEI/pDNA ternary nano-assembly was employed for probing the mechanism of association/ dissociation of polymeric carrier/plasmid DNA (pDNA) for efficient gene transfection. The probe was initially off due to quenching effect of Au on CDs. It was turned on upon ionic repulsion and Au-PEI disintegration under saline conditions.
Zhou et al. [159]	Multi-functional probe based on iron oxide nanocrystals and fluorescent carbon dots (CDs) were developed for MRI and fluorescent imaging. DOX was loaded so that the drug could serve as controlled chemotherapeutic agent. This alongside with the high tendency of CDs to convert NIR light to heat was employed for photothermal/ chemotherapy treatment.

CHAPTER 2

SCOPES AND EXPERIMENTAL METHODS

2.1 AIMS AND SCOPES

Primary tumor extermination and conventional chemotherapy are proved to be inefficient in cancer therapy in that they preferentially abolish differentiated cells whilst leaving behind treatment resistant, tumorigenic cancer stem cells (CSCs). CSCs are validated to be the root cause of therapeutic resistance, recurrence, and tumor progression. CSCs are considered to be modulated by overexpression of certain pathways including signal transducer and activator of transcription 3 (STAT3). Niclosamide (Nic), an FDA approved anthelmintic drug, has recently been reported as potent inhibitor of STAT3 and triggered the activation of cancer cell apoptotic mechanism [79]. Despite its promising cancer treatment capabilities, lack of solubility is a major drawback limiting its bio-availability. To circumvent the issue, we adopted a nanomedicine approach integrated with host-guest chemistry for sustained and enhanced delivery of this antineaoplastic agent traceable with vibrational spectroscopic method. The aim of this research is the synthesis and characterization of next generation luminescent carbon nanoparticles coated with cucurbituril for the controlled delivery of Nic as STAT3 inhibitor. In addition these particles can be tracked down by FT-IR and Raman imaging techniques therefore enabling their theranostic applications. Extensive physiochemical characterization has been carried out to elucidate the behavior of Nic in the presence of CB[6] and CNP. *In vitro* studies have been carried out to investigate the potential of the developed formulation for the drug delivery applications. The complex formation of Nic with CB[6] with sustained release ability is reported for the first time. In addition, carbon nanoparticles coated CB[6] as the delivery platform for the

enhanced cellular uptake and translocation of anti- cancer agent is developed for the first time in this research.

2.2 EXPERIMENTAL TECHNIQUES

2.2.1 MATERIALS AND REAGENTS

Food grade agave nectar was purchased from HoneyTree's® Organic Agave Nectar, Onsted, MI. Cucurbit[6]uril (CB[6]) hydrate (CAS Number 80262-44-8, Empirical Formula $C_{36}H_{36}N_{24}O_{12} \cdot xH_2O$) and Niclosamide, 98% (HPLC) (2',5-Dichloro-4'-nitrosalicylanilide, CAS Number 50-65-7) was supplied from Sigma Aldrich (St. Louis, MO, USA) and AKA Scientific Inc. (Union City, CA, USA), respectively. Nanopure water (0.2×10^{-6} M, 18 MΩ cm) was used throughout the experiment unless otherwise stated. For biological assessments, human breast cancer MCF- 7 cell line was obtained from American Type Culture Collection (ATCC) and was cultured using the prescribed instructions from the ATCC. High Glucose Dulbecco's Modified Eagle's Medium (DMEM; Sigma) was supplemented with 10% fetal bovine serum (FBS (Seradigm, US)) and 1% Penicillin Streptomycin (PenStrep) (Lonza) Trypsin (EDTA 0.02%, dextrose 0.05%, and trypsin 0.1%) in Dulbecco's phosphate buffer saline (DPBS, Gibco). Tetrazolium salt 3-[4,5-dimethylthiazol-2-yl]-2,5-diphenyltetrazolium bromide was prepared from Sigma. ^{1}H NMR measurements were carried out in DMSO-d6 (Cambridge Isotope Laboratories, Inc., MA, USA) as the solvent. Other reagents were obtained from Aldrich Chemical Co. (St. Louis, MO) and were used without further purifications.

2.2.2. PREPARATION OF NANO-CARBOBITACEAE

Pristine carbon nanoparticles (CNP) were synthesized by facile hydrothermal method using commercially available food grade agave nectar as the carbohydrate source. Agave nectar dispersed in water (0.2 mg.ml^{-1}) was slowly heated on a hotplate at 300 ºC (Corning®) so as to

evaporate water and the product visually changed color from amber to dark brown. Subsequently, the burnt residue was resuspended in water and probe- sonicated (Q700, Qsonica Sonicators, Newtown, CT) in the ice bath for 5 min at Pulsed Amp, 1; on, 5 s; off, 3 s. To obtain a narrow size distribution, the as synthesized nanoparticles were purified by dialysis cassettes using cellulosic membrane (10K MWCO, 3ml, Thermo Scientific, IL, USA) against nanopure (0.2×10^{-6} m) water for a prolonged period of time. Subsequently, the content underwent two steps of additional filtration (Acrodisc syringe) with mesh size of 0.45 μm and 0.22 μm, respectively.

Two methods of synthesis were applied for CB[6] decorated CNPs. In the first method, CB[6] was introduced on the surface of CNP *via* vigorous stirring of the respective concentrations of CB[6] for 5 min using vortex machine. These particles are labeled CB CNP post functionalized henceforth. In the second method, one pot nucleation of CB[6] CNP was carried out. Briefly, the mixture of agave nectar and CB[6] suspended in water at the desired concentration was hot plated and similar steps as for CNP preparation was followed. These particles are denoted as CB CNP prefunctionalized. Comprehensive physiochemical characterization of the prepared nanoparticles was carried out.

2.2.3 PREPARATION OF NANOFORMULATIONS

Stock of Nic was prepared in ethanol (2 mM) and then diluted with water to reach the desired concentration. The drug was loaded in nano-carbobitaceae using simple mixing method for 5 min.

2.3 DYNAMIC LIGHT SCATTERING MEASUREMENTS

The particles were mildly vortexed prior to size determination. The hydrodynamic size and the distribution of the nanoparticles was determined through dynamic light scattering measurements

on Malvern Zetasizer ZS90 instrument (Malvern Instruments Ltd, United Kingdom) at fixed angle of 90º. A photomultiplier aperture of 400 mm was used and the incident laser power was adjusted so as to obtain a photon counting rate between 200 and 300 kcps. The measurements whose measured and calculated baselines of the intensity autocorrelation function fell in +0.1% range were used to determine nanoparticle hydrodynamic diameter. The mean hydrodynamic diameter (Z-average) and polydispersity index (PDI) values were obtained based on the correlation function. PDI values below 0.3 are considered as unimodal size distribution with 0.2 indicating the monodispersed nanoparticles. All measurements were carried out in triplet of twelve consecutive measurements.

2.4 TRANSMISSION ELECTRON MICROSCOPY (TEM)

Prior to sample preparation for TEM imaging, the nanoparticles were mildly vortexed. 10 μL of sample was drop cast on 200-mesh copper grid. After 1 min, excess fluid was absorbed by lint free Kim wipes. The transmission electron micrographs were acquired on a JEOL 2100 Cryo TEM machine and imaged by Gatan UltraScan 2k × 2k CCD camera. The same concentration of CB CNP prefunctionalized and CB CNP postfunctionalized were used. The anhydrous diameter was determined by making 100 random measurements of nanoparticles on image J software (NIH, Bethesda, MD, USA) and was reported as mean± standard deviation.

2.5 ATOMIC FORCE MICROSCOPY (AFM)

An aliquot of nanoparticle suspension was placed on the top of freshly cleaved mica sheet attached to a stainless steel disc to minimize unwanted strains. Next, the specimens were vacuum dried overnight. AFM micrographs were obtained in the tapping mode on Asylum Cypher AFM device.

2.6 ELECTROPHORETIC POTENTIAL MEASUREMENTS

Zeta potential ζ values were determined using a Malvern Zetasizer (Malvern Instruments Ltd, United Kingdom) of nano series. The experiment was performed at 25 ºC and at PH=7 at the light scattering mode in the phase analysis light scattering (PALS) mode following solution equilibration at 25 °C. Calculation of ζ from the measured nanoparticle electrophoretic mobility (μ) employed the Smoluchowski equation: $\mu = {}^{\varepsilon\xi}/_{\eta}$ where ε and η are the dielectric constant and the absolute viscosity of the medium, respectively. Measurements of ζ were reproducible to within ±2 mV of the mean value given by 3 determinations of 15 data accumulations.

2.7 UV-VIS SPECTROSCOPY

Absorption spectra from different samples were recorded using GENESYS 10 UV-Vis spectrometer (Thermo Scientific, MA, USA). The samples were scanned in 220-800 nm range and the scan resolution was varied from 0.1-0.5 nm based on the requirements of the experiment. Experiments were carried out in 1cm plastic cuvettes with the covering wavelength range between 230-900 nm. Throughout all the experiments, the samples were diluted such that the solutions obeyed the Beer Lambert law to maintain highest accuracy. Concentration of a component of interest was determined based on carefully calibrated curves obtained by reading serial dilutions of the samples.

2.8 FOURIER-TRANSFORM INFRARED (FTIR) SPECTROSCOPY

As-synthesized particles were repeatedly applied to MirrIR IR-reflective glass slides (Kevley Technologies, Chesterland, OH, USA) to acquire IR spectra using a PerkinElmer Spotlight 400 (PerkinElmer, Waltham, MA, USA) equipped with a thermal source, and a raster-scanning linear array detector. Spectra were collected using a 1 $cm.s^{-1}$ mirror speed for acquisition, and zero

padding was not used. Background scans were taken at 8 cm^{-1} spectral resolution; 150 × 150 μm images were collected at 8 cm^{-1} spectral resolutions with 8 scans per pixel and a 6.25 × 6.25 μm pixel size. Data were atmosphere corrected on the spotlight and further processing was done using Matlab R2013 software.

2.9 RAMAN SPECTROSCOPY

Raman spectra were acquired on dried samples in reflection mode (LabRAM Horiba, as discussed above). The excitation wavelength for all measurements was 532 nm and the power was set to 25 mW at the sample with a 10 s acquisition time. The Raman shift from 400 to 4,000 cm^{-1} was collected at 8 cm^{-1} spectral resolution. Laser light was focused through a 100×, NA 0.8 objective into the sample plane and the scattering was collected in the reflection geometry using the spectrograph coupled with an Andor Newton back-illuminated EMCCD camera.

2.10 TRACKING THE COMPLEX FORMATION BETWEEN CB[6] AND NIC

2.10.1 STOICHIOMETRY OF THE REACTION

For the determination of the stoichiometry of the complexation event, Job's plot was constructed by plotting the amide peak wavenumber versus the mole fraction. The mole fraction of CB[6] was varied between 0 and 1 while keeping the total molar concentration constant at 0.5 mM. A total of 7 points were acquired for making the Job's plot. The extremum was taken as the Stoichiometric ratio.

2.10.2 UV-VIS TITRATION

1 ml of Nic (0.02 mM) in the mixed ethanol/ water solvent (1% v/v) was transferred to the UV-Vis cuvettes. Subsequently, 10 μL of titrant containing CB (0.3 mM) and Nic (0.02 mM) was added to the cuvette and mixed for one min. After each addition, UV-Vis spectra were obtained. The absorbance at 340 nm was plotted against equivalent of CB (i.e. [CB]/[Nic]).

2.10.3 FLUORESCENCE TITRATION

2D excitation, emission spectra were collected using a Horiba Aqualog Scanning Spectrofluorometer (Horiba scientific, Edison, NJ). 3000 µL of Nic (0.04 mM) was transferred to the cuvette and 2D excitation (240–700 nm) and emission (240-800 nm) contour was obtained at 3 nm resolution. Contribution of solvent was subtracted using nanopure water as the blank sample. After each measurement, the first- order Rayleigh scattering was corrected and all spectra were normalized to 1 $mg.l^{-1}$ quinine sulfate. Subsequently 30 µL of titrant containing Nic (0.04 mM) and CB[6] (0.6 mM) was added and mixed.

2.10.4 ^{1}H NMR TITRATION

^{1}H NMR measurements were carried out on Varian VXR 500 spectrometer operating at 500 MHz equipped with 5mm Nalorac QUAD probe. Chemical shifts were reported in ppm and referenced to the solvent proton impurities. DMSO-d6 was used as the deuterated solvent for all samples. 700 µl of Nic (2 mM) was transferred to the NMR tube. The temperature was raised to 37 ºC so as to ensure accurate shimming. A total of 128 acquisitions were made. Then 10 µl of titrant containing CB (30 mM) and Nic (2 mM) was added at each step and the acquisition was made. The data was processed and analyzed with MestRenova™ 8.1 software (Mestrelab Research SL; Santiago de Compostela, Spain).

2.10.5 MOLECULAR DYNAMIC SIMULATION

The ReaxFF-based Molecular dynamic simulations were implemented in order to figure out the energy minimized state between CB[6] and Nic. ReaxFF is a general bond order based empirical force field method which allows bond breaking and formation during simulations. The energy term is the superimposition of several contributions as follows:

$$E_{system} = E_{bond} + E_{over} + E_{under} + E_{lp} + E_{val} + E_{tor} + E_{vdWaals} + E_{Coulomb}$$

Where $E_{bond,}$ E_{over}, $E_{under,}$ E_{lp}, E_{val}, E_{tor}, E_{vdWaal}, $E_{Coulomb}$ are the energy contribution from bond, over-coordination penalty and undercoordination stability, lone pair, valence, and torsion, non-bonded interactions van der Waals, and Coulomb energies, respectively. In this method, the partial charge of the individual atoms are determined based on the electronegativity equalization method (EEM) to provide the geometry- dependent charge distribution [160, 161]. The minimization was carried out at 1 K using ReaxFF force field.

2.10.6 INTERACTION MONITORING BY ELECTROCHEMICAL MEASUREMENTS

The electrochemical of CB[6] and Nic and the CB[6], Nic complex in solution were studied by cyclic voltammetry on Reference 600™ potentiostat (Gamry Instruments, Warminster, PA). The sweeping range was -0.3- 1.2 V at the scan rate of 10 mVS^{-1} and initial/final potential of -0.3/1.2 V respectively. The stock of Nic in ethanol (2 mM) was diluted by phosphate buffer saline (0.1 M, pH 7.4) to reach to the concentration of 0.05 mM. Similarly CB was dispersed PBS. The corresponding volumes of CB and Nic were vortexed to reach the desired concentration. The experiment was carried out at room temperature using gold macrodisc electrode as the working electrode. The data were referenced against Ag/AgCl electrode and platinum was chosen as the counter electrode. Prior to each set of experiment, open circuit potential (OCP) measurement were taken to assess the stability of the solutions.

2.10.7 PH TITRATION TRACED BY UV-VIS SPECTROSCOPY

To monitor the effect of CB[6] on the pKa value of Nic, pH titration study was adopted. Initially Nic (0.02 mM) was prepared in 100 ml of low pH water (adjusted by addition of HCl). The pH was carefully adjusted by concentrated aliquots of NaOH and 1 ml of sample at specific pH was taken. The absorbance profile was collected by UV-Vis spectroscopy machine. The same

procedure was followed for Nic (0.02 mM) in the presence of CB (0.2 mM). The concentration of CB was chosen so as to ensure the excess of CB.

2.11 IN VITRO ASSESSMENTS:

2.11.1 PARTICLE STABILITY UNDER PHYSIOLOGICALLY RELEVANT CONDITIONS

Stability of the formulation was monitored over a period of 30 days by evaluating the hydrodynamic diameters at different time points. The particles were incubated at three different conditions namely, aqueous solution with pH=7.4, aqueous solution with pH 4.5 (to mimic cancer cell environment) and aqueous solution containing 10% FBS. The samples were kept in water bath cycled to 37 ºC and were taken out for DLS reading at the corresponding time intervals.

2.11.2 DRUG LOADING EFFICIENCY

The loading efficiency of Nic in CB[6] was calculated by measuring the concentration of unbound drug. The samples were vigorously centrifuged (Optima™ MAX-XP Ultracentrifuge, Beckman-Coulter, Brea, CA) for 10 minutes at 75,000 rpm. Subsequently, the supernatant was collected for further analysis. The concentration of the unbound drug was determined by UV-Vis analysis of the collected supernatant and interpolating the concentration on the constructed calibration curves of known Nic concentration. Following equation was utilized for loading percentage determination:

% Loading efficiency= [(Loaded niclosamide– Unbound niclosamide)/Loaded niclosamide]*100.

2.11.3 DRUG RELEASE KINETIC STUDY

The *in vitro* drug release profile were monitored under various physiologically relevant conditions and prolonged for 120 hours. Specifically, three conditions were adopted: 1. pH=7.4,

25 ºC, 2. pH=4.5, 37 ºC, 3. pH=7.4, 37 ºC 4. Aqueous media, 10% FBS, 37 ºC (the experiment was hindered due to high inconsistency in the UV-Vis pattern). 1 ml of CB [6] (10^{-3} mM), CB [6] (10^{-3} mM) CNP (pre functionalized) and CB [6] (10^{-3} mM) CNP (post functionalized) containing 0.1 mM Nic was pipetted into a dialysis cassette (10K MWCO, 3ml, Thermo Scientific, IL, USA) and dipped into 100 ml of the media to simulate sink condition. The beaker was magnetically stirred to keep the conditions homogenous across the solution. At the specified time points, 1 ml of the sample was taken for further UV-Vis analysis. The media was supplemented with 1 ml of fresh media to maintain the volume. The concentration of the released load was determined using calibration curves.

2.11.4 IN VITRO CELLULAR CYTOTOXICITY STUDIES

Cell toxicity assay was performed on human breast cancer ER (+) MCF-7 (ATCC) cells. Cells were cultured in Dulbecco's modified Eagle's medium supplemented with 10% fetal bovine serum (FBS) in T25 culture flasks (Cellstar; Germany) and were incubated at 37 °C in a 99% humidified atmosphere containing 5% CO_2. Cells were regularly passaged by trypsinization with 0.1% trypsin (EDTA 0.02%, dextrose 0.05%, and trypsin 0.1%) in DPBS (pH 7.4). Nonsynchronized cells were used for the experiments.

2.11.5 CELL VIABILITY ASSESSMENTS

The cell toxicity assay measures the potency of the drug in inhibiting the cell growth and compared by calculating IC_{50} (inhibitory concentration for 50% cell population). MCF-7 cells were seeded in the 96- well- tissue culture polystyrene plates with the density of 10^4 cells per well. After 24 h the cells were treated with the samples prepared in growth medium at various concentrations ranging from 1.5-50 μM. After 44 h of incubation, cells were imaged for bright field imaging to visualize the effect of treatments on cell growth density and changes in cellular

morphology. It was followed by addition of a 20 µl (5 $mg.ml^{-1}$) solution of MTT to the growth medium while growing the cells. MTT turns into purple formazan after reduction by mitochondrial enzymes in living cells. MTT added cells were incubated for 4 h at 37 °C under 5% CO_2 atmosphere. The solution was removed and replaced by 200 µl of dimethyl sulfoxide (DMSO) added to each well and incubated for another 5 min. The solution was mixed by pipette in order to completely dissolve the dark blue crystals from the samples. Absorption was read on multi-well plate reader machine (BioTek Synergy HT, US) using the standard wavelengths of 592 nm. An average of the triplicate wells were calculated and normalized by dividing to the value of control well, the standard error mean was calculated for each sample using software Graph pad prism 6.0.

CHAPTER 3

RESULTS AND DISCUSSION

3.1 PARTICLE SYNTHESIS AND GENERAL CHARACTERIZATIONS

The selectivity of drugs towards the cancerous cells is one of the limiting factors in the application of current chemotherapeutic agents. The therapeutic window for the conventional anti-cancer drugs is low which implies that higher dosage would require inducing a certain therapeutic effect. This raises the concerns about off- target toxicity. Drug resistance is another problem during chemotherapy which mandates the application of combination therapy or increased dosage of the drug. In order to suppress the chemotherapy- related problems, various nanomedicine systems such as, micelle and drug polymer conjugates have been developed where a plethora of research interests have been directed towards nanoparticles due to their extraordinary properties such as their high surface to volume ratio, their favorable safety profile, their tendency to cross cellular barriers and their flexibility in surface functionalization by moieties for targeted applications. An emerging application of nanoparticles as "theranostic" agents, the marriage of therapy and diagnostics, further entices scientists to delve into their unique properties as they offer advanced capabilities in a single platform. Despite the promising properties of nanoparticles, their translation from bench to bedside is not a trivial issue and requires extensive characterization in terms of biocompatibility, pharmacokinetics, reproducibility and real time monitoring of the drug release [162]. Towards this end we adopted a facile green route where we moved away from harshly chemical synthetic modifications to obtain our pristine carbon nanoparticle. The carbohydrate source was chosen as agave nectar

which has a high fructose and glucose level further ameliorating the safety issues relevant to nanoparticle toxicity. In the next step, we adopted a facile approach for the introduction of CB[6] on CNP surfaces because it was predicted that the physio-absorption would anchor CB[6] on the surface CNP through hydrogen bonding. In the final step, Nic as the cancer stem cell targeting therapeutic was introduced to the system through non covalent interaction. The overall adopted procedure is demonstrated schematically in Figure 3.1.

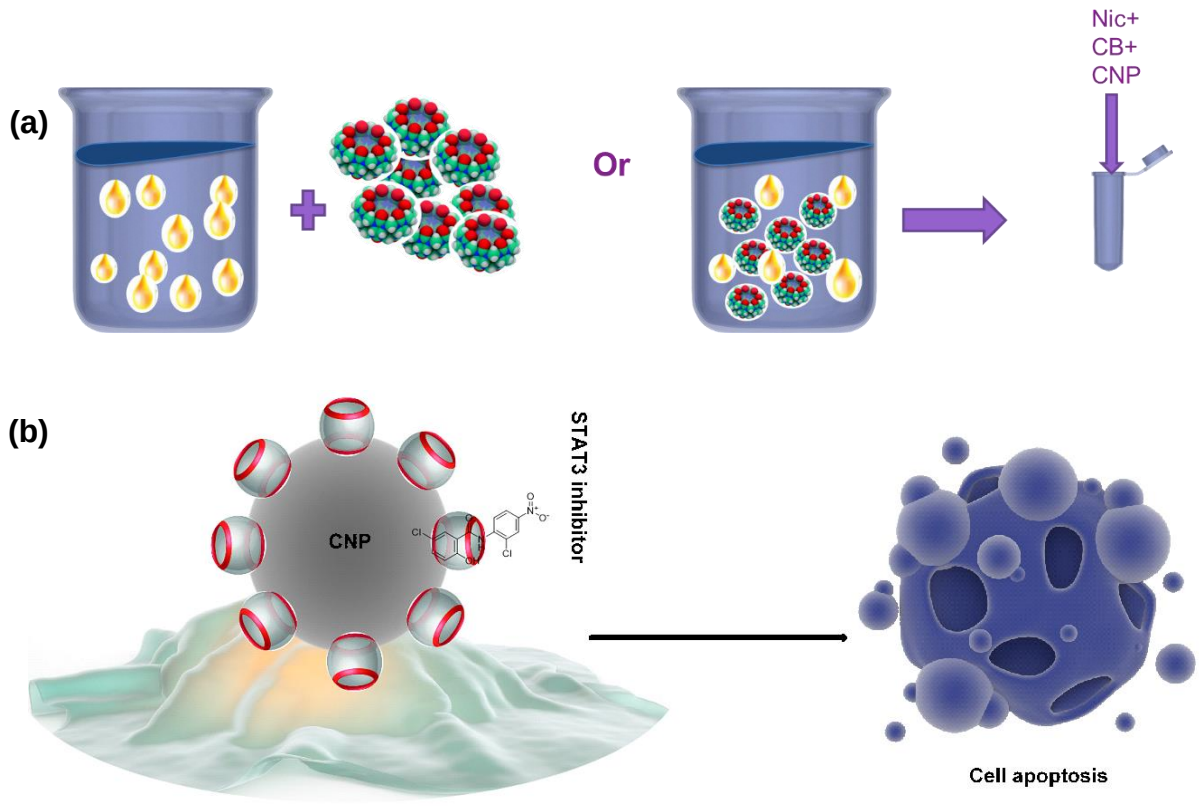

Figure 3. 1 (a) The particles were prepared by two methods i.e. either post functionalized (left) or pre functionalized (right); niclosamide was introduced to both particles subsequently by vortexing; (b) The CNP coated with CB[6] loaded with STAT3 inhibitor (niclosamide) can effectively target cancer stem cell and lead to cell apoptosis.

It is important to determine the hydrodynamic size of the nanoparticles for systemic applications as it directly influences the nanoparticles accumulation and clearance profile from

body. Therefore, dynamic light scattering measurements were carried out for pristine and functionalized particles. Initially, the hydrodynamic size of the prepared carbon nanoparticles decorated with CB[6] was optimized by making various dilutions of CB[6] while keeping the CNP content constant. The ultimate goal was to reach a monolayer of CB[6] on the top of the nanoparticles. As can be seen in Figure 3.2 the concentration of CB[6]=10^{-3} mM yielded the optimum hydrodynamic size whilst further dilution of CB[6] resulted in no significant size variation implying the optimal condition. Hence, the concentration of CB[6] was set to 10^{-3} mM in the rest of the experiments.

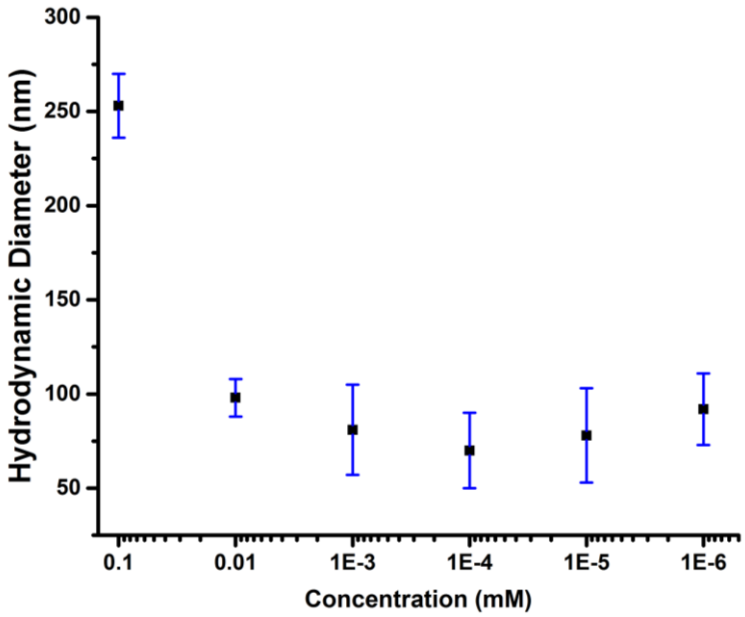

Figure 3. 2 Optimization of the hydrodynamic diameter through serial dilution.

Two methods were adopted for the preparation of CB[6] decorated CNPs. The hydrodynamic size obtained by the methods was compared using dynamic light scattering. The mean hydrodynamic size for CNP, CB[6] CNP post functionalized and pre functionalized samples was determined to be 76±13, 93±4 nm and 55±1 nm, respectively (Figure 3.3a). The small size

difference between CNP and CB[6] coated samples showed that CB[6] did not appreciably affect the size and presumably resulted in the formation of single layer coating. Similarly, the anhydrous size diameter was determined after 100 random measurements through TEM analysis and it was revealed that the size was 88±22 nm and 31±6 nm for post and pre functionalized samples, respectively. As shown in Figure 3.3b, the discrepancy between hydrodynamic and anhydrous diameter was marginal suggesting the semi rigid nature of these particles. In fact, the hydrodynamic size is seen to be greater in the soft particles such as polymers which tend to entrap high water content in their structure; yet in the case of hard core particles the difference is negligible. The smaller size of prefunctionalized samples compared to post functionalized ones could be due to more controlled nucleation of CNPs in the presence of CB[6] as a result of confinement effects CB[6] exerts on CNP growth.

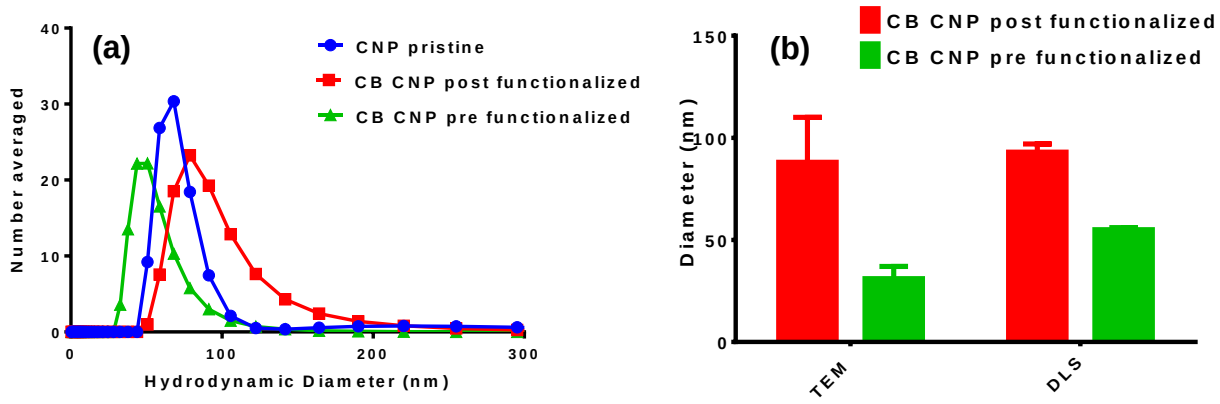

Figure 3. 3 (a) The hydrodynamic size comparison between CNP, CB[6] coated CNP pre and post functionalized, (b) the comparison between anhydrous and hydrodynamic size of the CB[6] coated CNP obtained by two method of synthesis.

One limitation associated with the applications of nanomaterials in biomedicine is their tendency to form agglomerate in high- ionic strength solutions such as biological media as a result of pronounced effect of particle functionalities. Therefore, it is of prime importance to investigate the nanoparticle size stability over extended period of time so as to avoid potential issues such as blockage of blood capillaries *in vivo* and elimination as foreign entities by reticuloendothelial system (RES) [163]. The stability of the nanoparticles was examined at various physiologically relevant media over the period of one month (Figure 3.4a-c).

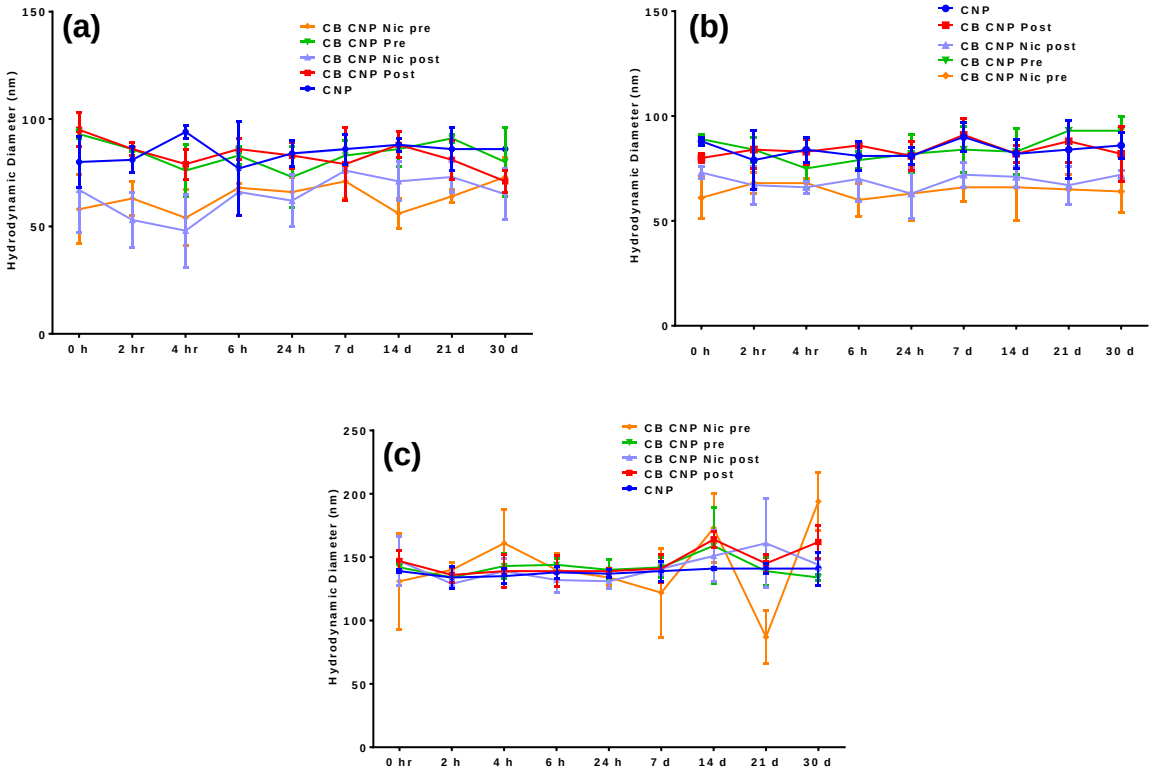

Figure 3. 4 Stability profile based on hydrodynamic size monitored in the period of one month in (a) aqueous media, (b) aqueous low pH environment, (c) aqueous media containing 10% FBS.

The hydrodynamic size measurement revealed that particles were quite stable without any noticeable aggregation in aqueous media at neutral pH and aqueous media at pH 4.5 at 37 ºC. Interestingly, the particles incubated in aqueous media containing 10% FBS also demonstrated a stable profile. FBS is a widely used serum in cell culture studies because it closely mimics the protein contents and properties of biological fluids [163]. It should be noted that the DLS size reading based on count criteria was hampered due to the masking effects of FBS macromolecules on size and instead the intensity criteria was chosen for size measurement in FBS containing media. This much of stability at various media can be attributed to the negative zeta potential values which result in particle repulsion and prevent aggregation.

The morphology and size distribution of the nanoparticles are illustrated in Figure 3.5 a-d. A bright halo ring around post functionalized samples clearly indicated the formation of uniform coating around CNP (Figure 3.5c). Furthermore, the particles prepared in the presence of CB[6] showed network formation into several clusters (Figure 3b, inset). This could be due to CB[6] assisted self- assembly as has already been pointed out for gold nanoparticles [164]. For our system, we hypothesized that the growth of CNP was possibly mediated through the binding of carbon atoms onto the carbonyl portal of CB[6] which glued the CNPs together. The particles were further characterized by AFM measurements (Figure 3.6) where the average height of both post and prefunctionalized samples were determined to be approximately 20 nm.

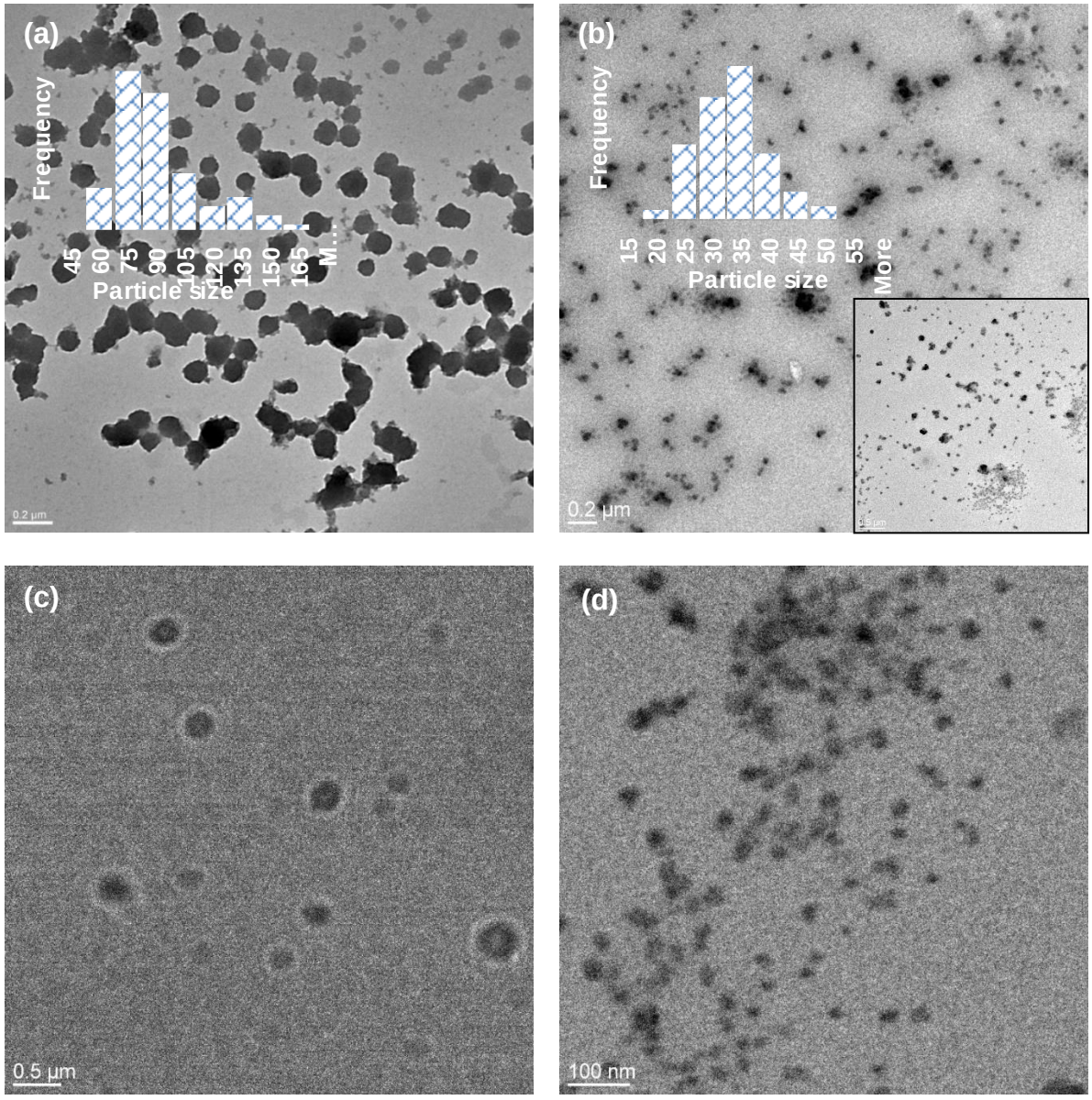

Figure 3. 5 Transmission electron micrographs of the prepared nanoparticles; (a) and (c) post functionalized CB[6] coated carbon nanoparticles, (b) and (d) pre functionalized CB[6] coated nanoparticles.

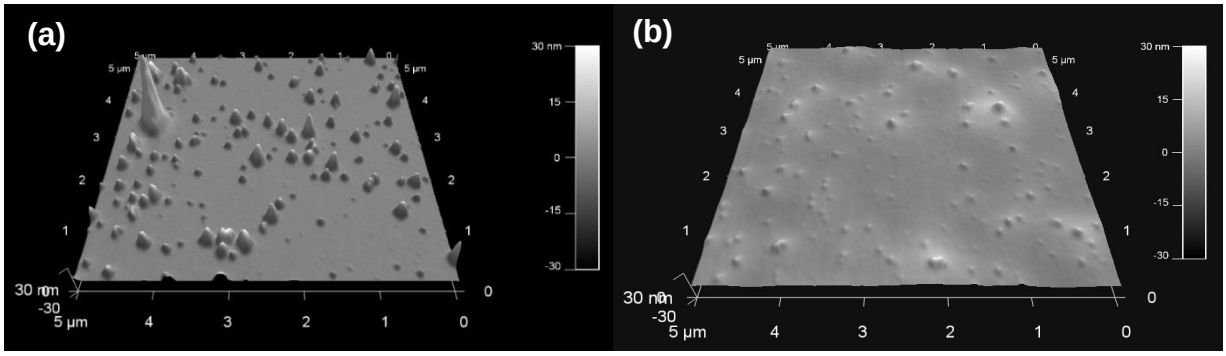

Figure 3. 6 Tapping mode AFM topographical images of (a) post and (b) pre functionalized carbon nanoparticles.

In the next step, the electrophoretic potential of the pristine CNP and CB[6] CNP in the absence and the presence of Nic were determined by zeta potential measurements (Figure 3.7). The negative zeta potential on the surface of CNP (-29 ± 5 mV) represented the abundance of carboxyl, carbonyl, hydroxyl groups which contribute to the enhanced aqueous dispensability and stability of CNPs and would therefore facilitate the *in vitro* and *in vivo* applications In the presence CB[6], zeta potential values became slightly more positive both for postfunctionalized (-27±5 mV) and prefunctionalized samples (-19±9 mV) which is consistent with the surface charge on the outer surface of CB cavity carrying slightly positive charge [165]. Also, the addition of Nic further contributed to higher zeta potential values (-18±5 mV for drug loaded postfunctionalized, -20±4 mV for prefunctionalzed samples, respectively). This observation could be as a result of the electrostatic interaction of CB[6] and Nic and complexation event which masked the negatively charged groups on Nic and imparted a positive charge. However, the values still lied in the stable range and the electrostatic repulsive forces sustained the colloidal stability to prevent the agglomeration of CNP. This observation was further supported by the DLS measurements in various physiologically relevant environments over the course of one month.

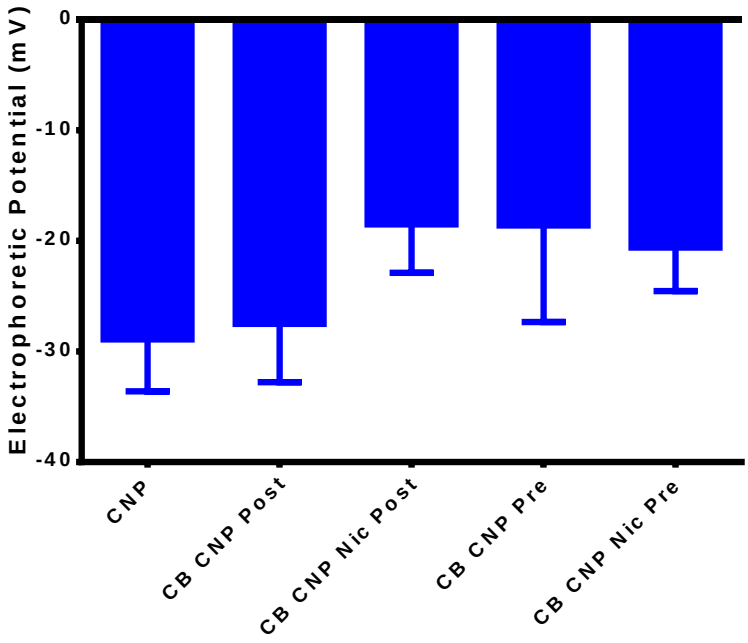

Figure 3. 7 Electrophoretic potential (ζ, surface charge (mV)) from zeta potential measurement.

The UV-Vis spectra of CNP, Nic, CB[6] CNP pre functionalized, CB[6] CNP post functionalized sample in the absence and the presence of drug is shown in Figure 3.8a. The absorption band for CNP was seen to be monotonically increasing and was devoid of any band gap transition that is typical of amorphous carbon substrates. In fact, the peak at around 280 nm can be attributed to the n–π* transition of the C=O band and the π–π* transition of the conjugated C=C band. CB[6] did not show any UV-Vis signature peak due to the lack of conjugated moieties. Nic, on the other hand, showed UV-Vis spectrum which was dependent on the pH of the experiment. Figure 3.8b showed the effect of pH on the peak positions of Nic. Nic was barely soluble in water and low pH conditions while its solubility was greatly enhanced by increase in pH. At basic pH, Nic indicated four distinct peaks whereas in acidic or neutral conditions only two bands appeared which could be explained based on the resonance effects as well as the dissociation of phenolic- OH group to phenolate in base [58]. In addition, from Figure

3.8a it is evident that the addition of CB[6] resulted in dampening of Nic characteristic peaks confirming complexation between Nic and CB[6]. In the same vein, CB[6] CNP postfunctionalized samples also showed similar trend. Furthermore, UV-Vis studies on drug loaded particle were carried out. As can be seen (Figure 3.8a) the characteristic hump of Nic at 377 nm was apparent in drug loaded CB[6] CNP particles and was mostly masked by the CNP spectrum. The tracking of the complexation between CB[6] and Nic is further elucidated by various titration methods which will be discussed in details in subsequent chapters.

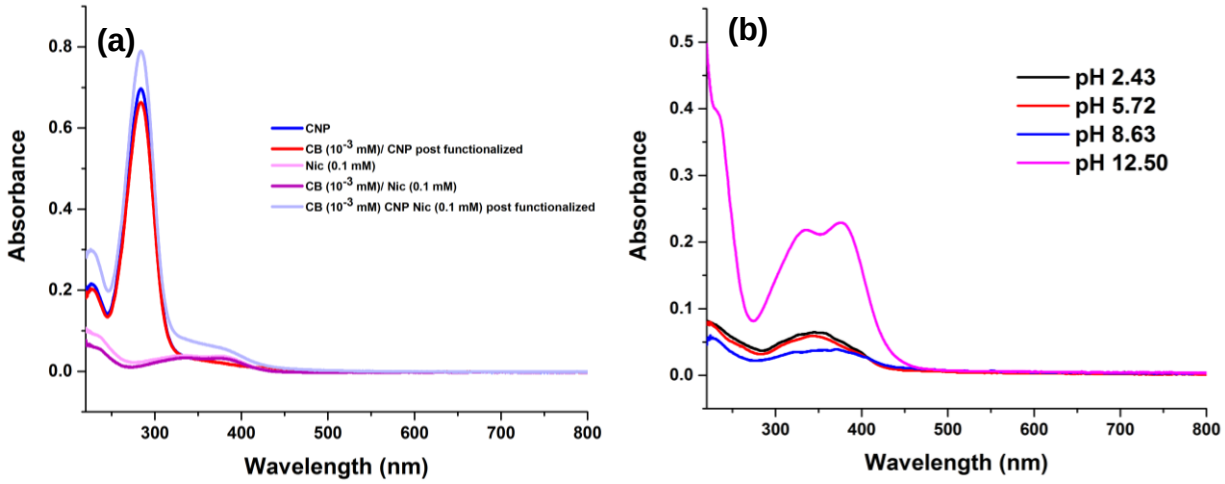

Figure 3. 8 UV-Vis spectra of (a) the individual components and their interactions (b) niclosamide at various pH.

Vibrational spectroscopy is a powerful method in identifying the interaction between various components in the system. Figures 3.9a and b show the FTIR and Raman spectra of pristine CNP along with prefunctionalized and postfunctionalized samples with CB[6] in the presence and absence of Nic. Characteristic features of both Nic and CB[6] can be identified from both of the spectra. For the IR characterization, we focus on the $\nu_{C=O}$ (1680 cm^{-1}), ν_{AmideI} (1550 cm^{-1}), $\nu_{C=C}$, ν_{NO2} (symmetric and asymmetric) stretch for the Nic molecule. The

characteristic band assignment of CB[6] was also made as follows: 1732 cm^{-1} C=O [166], 3485 cm^{-1} N-H [167], 1473 cm^{-1} C-N stretching vibration [167] and 2930 cm^{-1} $-CH_2$ stretching vibration [168].

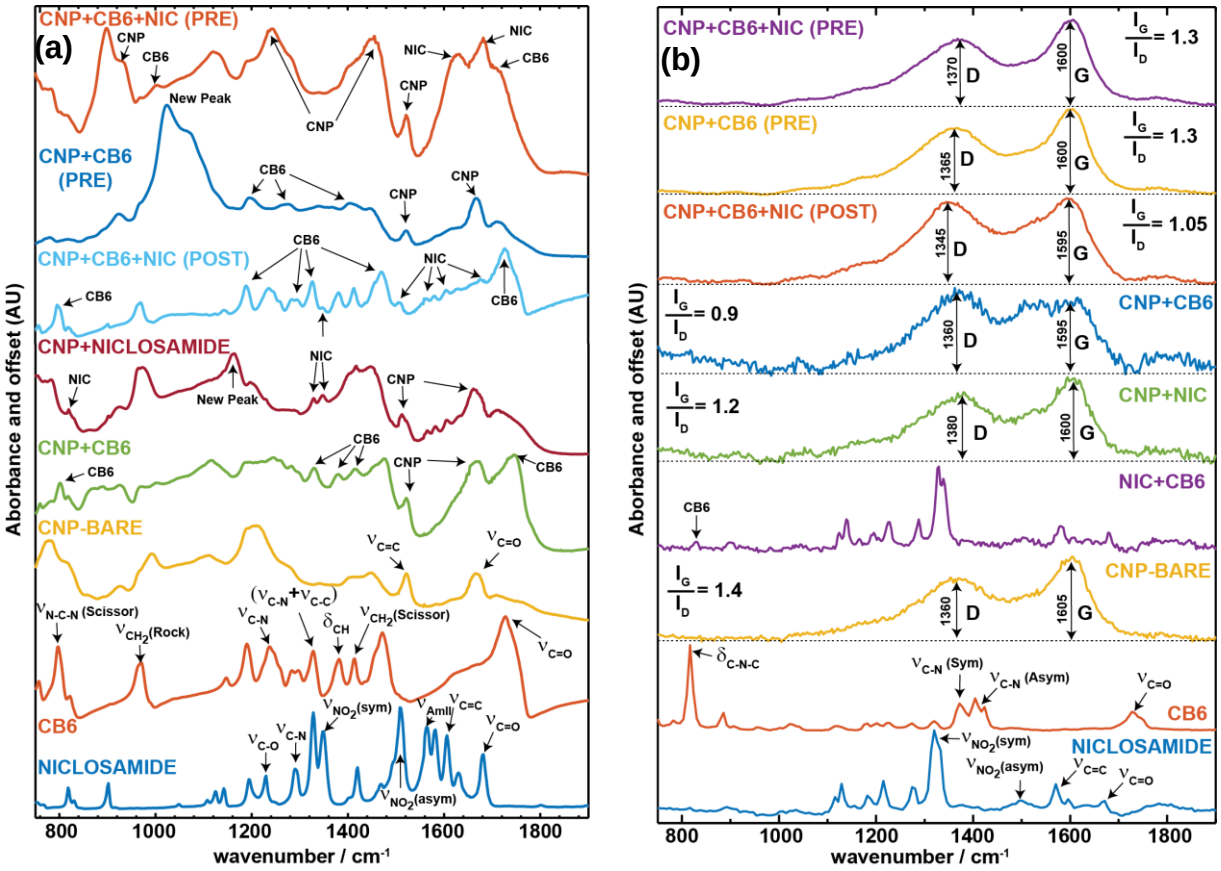

Figure 3. 9 (a) Infrared absorption and (b) Raman spectra of various formulations. In the Raman spectra of the CNP samples the D and G bands are taken as an indicator of the successful functionalization.

Pristine CNPs had a variegated structure, which depended on the choice of synthesis precursors. CNPs displayed a variety of IR peaks including $\nu_{C=O}$ and C=C vibrations. Upon CB[6] and/ or Nic introduction on the CNPs surface, features corresponding to both Nic and CB[6] can be identified. This is a proof of successful incorporation of the molecules on the CNPs surface and also confirmed the successful implementation of the synthetic strategy. To compare the synthetic

routes to functionalize the CNPs with CB[6] and Nic, the IR spectra of the products from the pre and post functionalized syntheses were investigated. While in the post functionalized samples, CB[6] and the Nic peaks can be easily identified, the CNP features were less distinct. On the other hand, in the pre functionalized samples, the CNP features overwhelm the vibrational peaks from Nic and CB[6].

While the molecular vibrational features from each of the components (Nic and CB[6]) were distinct in infrared, the intense Raman features corresponding to the CNPs masked the contributions from the other passivating molecules. CNPS are interesting materials to be imaged by vibrational spectroscopy in biological settings. Therefore, they can be utilized as a platform for theranostics applications to track the distribution of drug inside the organisms and to optimize disease treatment [162, 169]. The two characteristic bands of CNPs i.e. D and G bands are utilized to this end. The D band (sp^3 hybridized) is often referred to as the disorder band or the defect band and is associated with the vibration of carbon atoms with dangling bonds in the terminal plane of the disordered graphite of amorphous carbon. The G band (sp^2 hybridized), on the other hand, is related to the vibration of carbon atoms in a two dimensional hexagonal lattice [170]. The ratio of the two parameters was used as an indicator for the determination of the structure of CNPs. We identify the extent of passivation through the ratio of the G and D bands, which showed a considerable change with the change in the nature of the passivation. The change could be attributed to the collective addition of all the molecular vibrational features in the 1200-1400 cm^{-1} region which affected the intensity ratio.

3.2 TITRATION STUDIES

A very critical parameter during complexation event is the binding constant which is indicative of the stability of the complex. The terms binding constant, stability constant and equilibrium

constant are interchangeably used in the context of host guest chemistry and are is determined *via* various analytical tools. In this research, we used UV-Vis spectroscopy, fluorescence spectroscopy, ^{1}H NMR spectroscopy and cyclic voltammetry to investigate the complexation event between Nic and CB[6]. The rationale behind using various analytical methods originates from the fact that the host (H) guest (G) chemistry of CB[6] and Nic is unexplored and to the best of our knowledge this is the first study on this system. Titration studies were carried out utilizing these analytical techniques. In a typical titration investigation, the concentration of one component (i.e. either guest or host) was kept constant while the concentration of the other component was varied. To ensure the maintenance of the concentration in the titrant, a solution containing both host and guest is prepared where the concentration of host was 10-20 times greater than the host concentration. Therefore, upon the addition of aliquots of the titrant the concentration of host was gradually increasing whilst keeping guest concentration constant. A parameter such as absorption in UV-Vis spectroscopy or ^{1}H NMR shift was tracked which was directly proportional to the concentration of [HG] complex. Finally, depending on the stoichiometry of the reaction, relevant kinetics and thermodynamics parameters were obtained.

3.2.1 STOICHIOMETRY OF THE REACTION BY THE METHOD OF CONTINUOUS VARIATION

In order to determine the stoichiometry of a reaction, the method of continuous variation was utilized where the molar fraction of one the components (i.e. $\frac{[H]_0}{[H]_0+[G]_0}$) was varied between zero and one and the concentration of [HG] (which was tracked by one concentration dependent parameter) was plotted versus mole fraction. The maxima or minima of the graph (Job's plot) determines the stoichiometry of the reaction. The constructed FT-IR Job's plot is demonstrated in Figure 3.10b. While most of the vibrational modes corresponding to both Nic and CB[6] remained constant (Figure 3.10a), the amide II modes (C-N) shifted to lower energies at a 2:3

concentration ratio corresponding to CB[6] and Nic. A possible reason for this could be due to the favorable interaction between the Nic molecules when it is inside the cavity of CB[6]. However to ascertain these interactions ab-initio calculations are needed to be carried out.

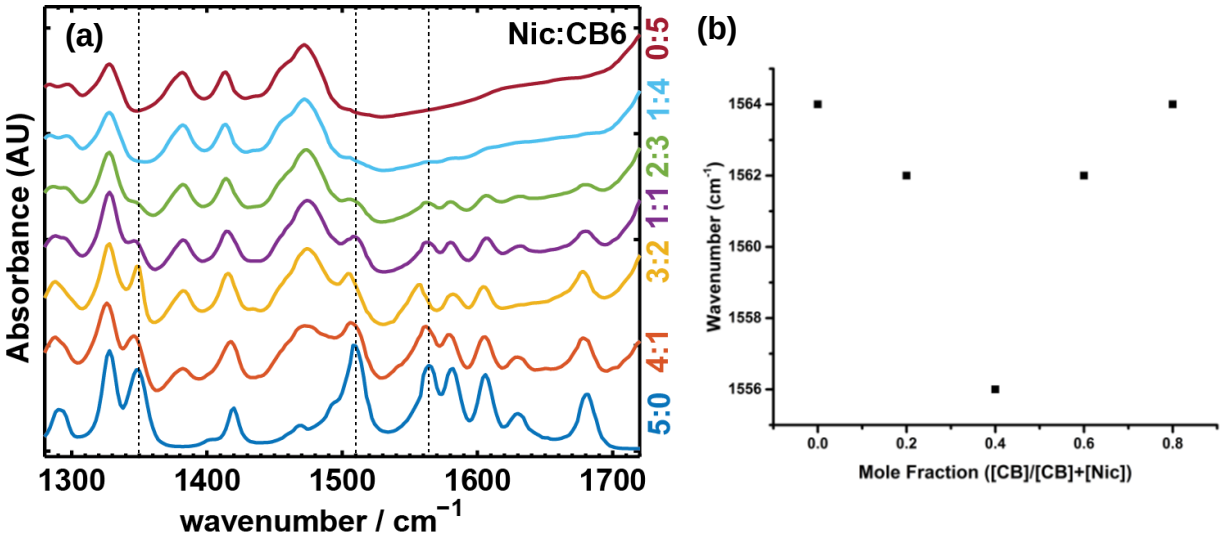

Figure 3. 10 (a) FTIR spectra for varying molar ratios of CB and Nic, (b) Job's plot showing the 2:3 binding model.

3.2.2 UV-VIS TITRATION

Details of carrying out a proper UV-Vis titration have been delineated already. The absorption for the peak at 340-343 nm is plotted against the [CB]/[Nic] concentration (Figure 3.11 a-d). The experiment was attempted twice by different machines. However, the determination of binding constant was hindered due to the strong scattering on the part of CB[6]. It has to be mentioned that the threshold for the scattering effect is approximately at the [CB]/[Nic]=1 which suggests that the unbound CB species were not creating significant scattering issue and the excess of CB after the mentioned threshold seriously affected the determination of the parameters of interest.

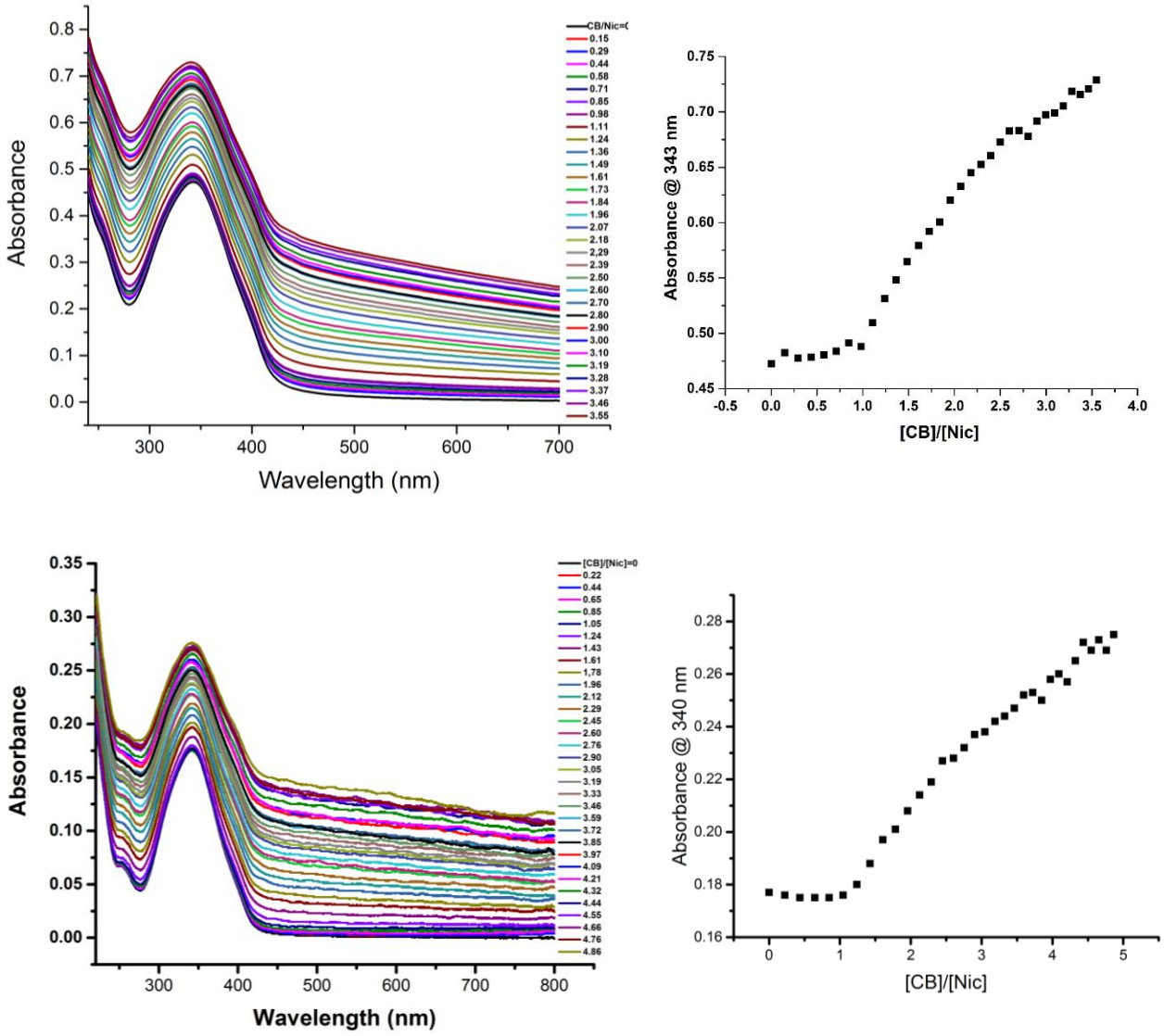

Figure 3. 11 UV-Vis titration curves of Nic with CB[6] collected by two different machines (a) Horiba Aqualog Scanning Spectrofluorometer (c) GENESYS 10 UV-Vis spectrometer, (b) and (d) host guest interaction by measuring absorbance at the respective wavelength.

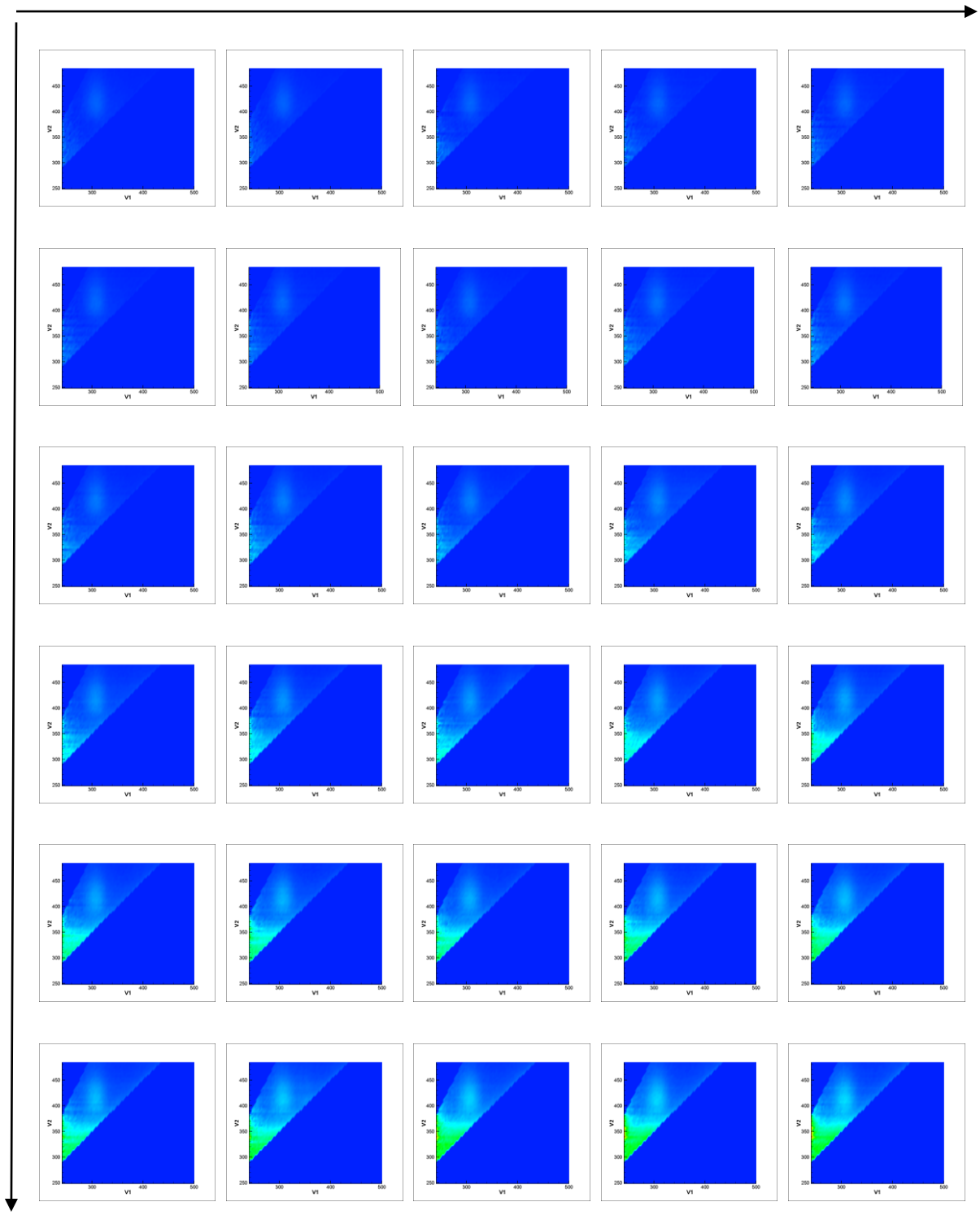

Figure 3. 12 The fluorescent titration of Nic with CB[6] observing the scattering pattern. The arrows indicate the increase in concentration of CB[6].

The same issue with strong scattering due to low insolubility of the system was encountered with fluorescent titration (Figure 3.12). Nic lacks inherent fluorescence properties and therefore might not be the best candidate for carrying out the fluorescent titration. As expected, the fluorescence titration experiment did not yield any interesting patterns, although a gradual and consistent upward shift in the scattering intensity pattern was noticed. Therefore, we assumed that NMR titration which is not affected by the scattering of CB[6] should help us revealing the nature of binding more appropriately.

3.2.3 ^{1}H NMR TITRATION

NMR is a very powerfulmethod for acquiring information regarding the mechanism and structural location of the complex formation in the supramolecular chemistry. For instance, it may reveal which protons are encapsulated and which ones are not. Specifically, guest protons resonances located within the CB[6] cavity would experience an upfield shift (lower ppm) due to shielding effects whereas the protons outside the CB[6] portal would shift slightly downfield (higher ppm) due to deshielding effects. Thus, changes in chemical shift of the drug resonances, together with changes in line width, give information on the location, orientation and the kinetics of the binding of a drug bound to CB[6].

First and foremost, the assignment of the peaks was made in Nic ^{1}H NMR spectrum (Figure 3.13). The peaks obtained by experiment were compared with the results from the reported chemical shifts. The results are summarized in Table 3.1.The titration curves are shown in Figure 3.14. Interestingly, after the addition of 0.028 mM of CB[6], pronounced splitting and broadening was noticed in the characteristic Nic peaks. This can be associated with the presence of mixed magnetic species of Nic as a result of complexation with CB cavity. In other words, the species interacting with CB[6] are experiencing a different electronic environment as a result of

interaction while the uncomplexed species remained unaffected at lower concentrations. This observation virtually disappeared upon further addition of Nic suggesting the magnetic homogenization of the species. The titration revealed that the amide peak moved downfield. One explanation for this observation might be due to the keto-enol tautomerisation where the N-H bond can be replaced by more electronegative OH bond and therefore the corresponding peak shifted downfield and the Nic got stabilized upon encapsulation. In addition, the protons # 1, 5, 16 and 17 were all shifted upfield suggesting encapsulation by CB[6] whereas proton #19 shifted downfield due to being sticking out from CB[6] cavity. The suggested orientation was further confirmed by molecular modelling energy minimized studies of the CB and Nic. The energy minimized orientation of the Nic in CB cavity is shown in Figure 3.15a-c.

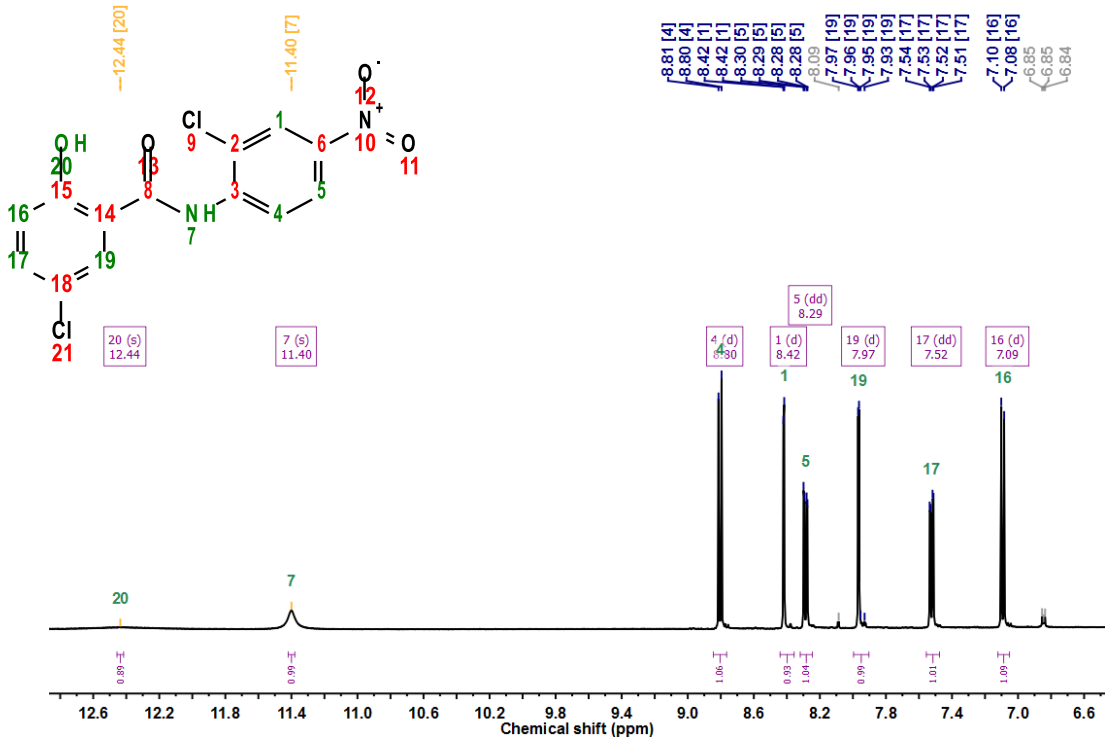

Figure 3.13 Peak assignments of niclosamide.

Table 3. 1 The observed chemical shift of the numbered protons and its comparison by the literature data.

Proton #	Observed Chemical Shift (ppm)	Literature data [58]	Multiplicity
4	8.81	8.82	doublet
1	8.42	8.45	doublet
5	8.29	8.30	doublet of doublets
16	7.08	7.10	doublet
17	7.52	7.55	doublet of doublets
19	7.98	7.97	doublet

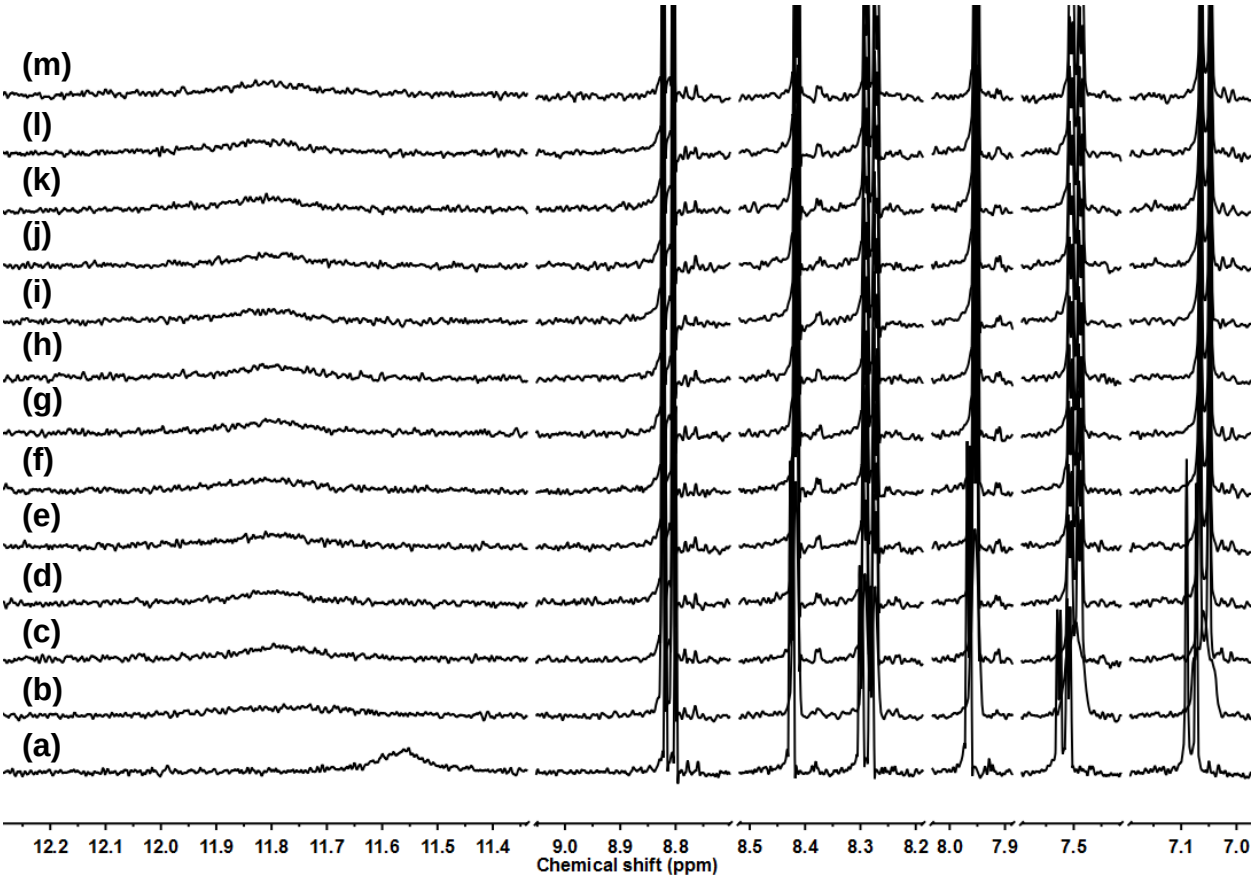

Figure 3. 14 The ^{1}H NMR spectra of niclosamide (2 mM) in the (a) absence and presence of (b) 0.21, (c) 0.42, (d) 0.62, (e) 0.81, (f) 1.00, (g) 1.18, (h) 1.36, (i) 1.54, (j) 1.71, (k) 1.88, (l) 2.04, (m) 2.20 equivalent of cucurbituril [6].

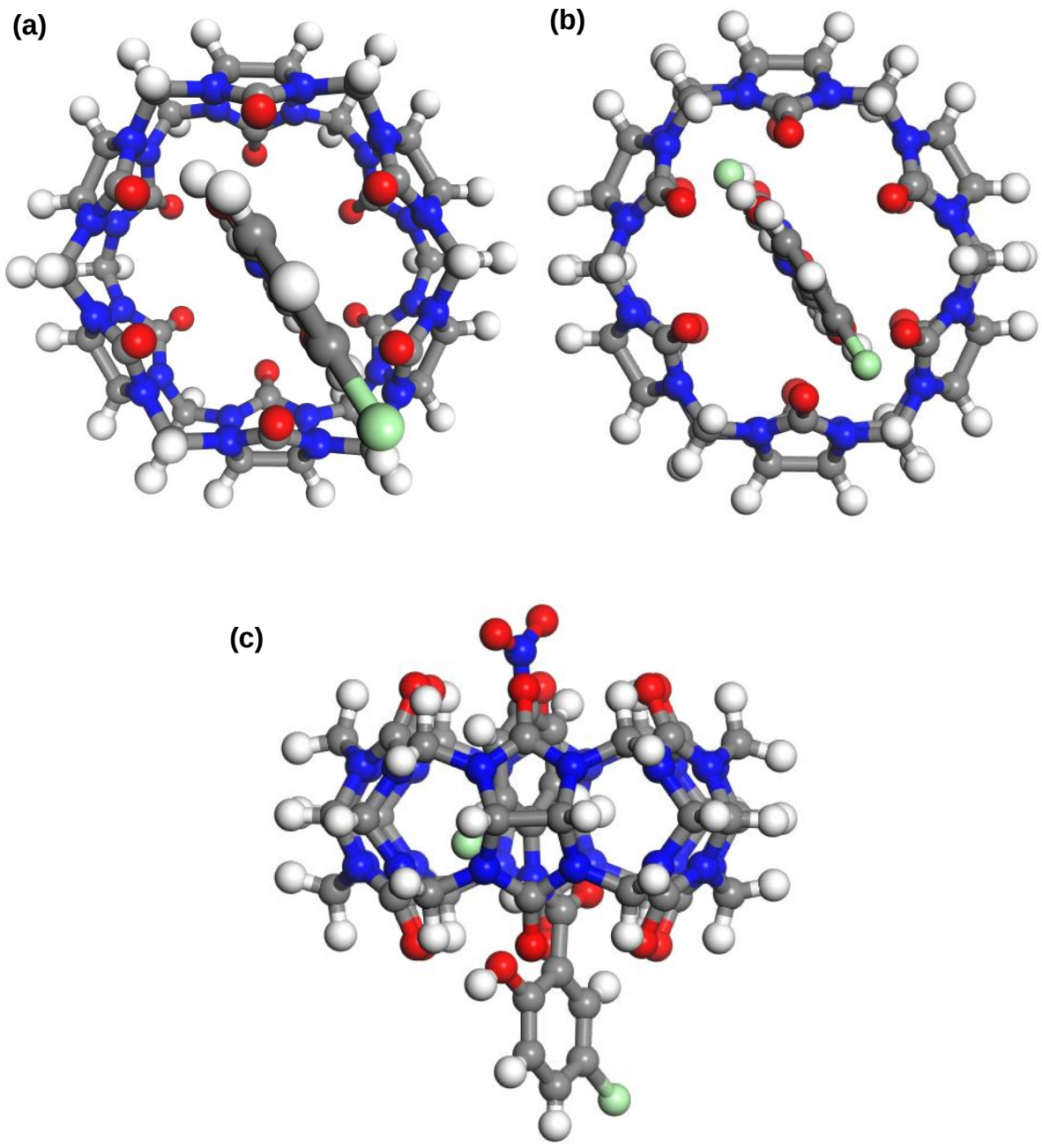

Figure 3. 15 Possible energy minimized configuration of Nic in CB[6] cavity. (a) Perspective, (b) orthotropic and (c) front view. The colors white, red, blue and green correspond to hydrogen, oxygen nitrogen and chlorine respectively.

Besides, it was seen that the peak at 3.33 which is attributed to water peak was shifted downfield (Figure 3.16). In fact, the first guest molecule that was proven to be encapsulated in hydrophobic CB cavity was water molecule [171]. Upon complexation, water molecule was released from the CB cavity and therefore, the peak moved downfield to the deshielded region. Similar behavior has been reported elsewhere [172, 173].

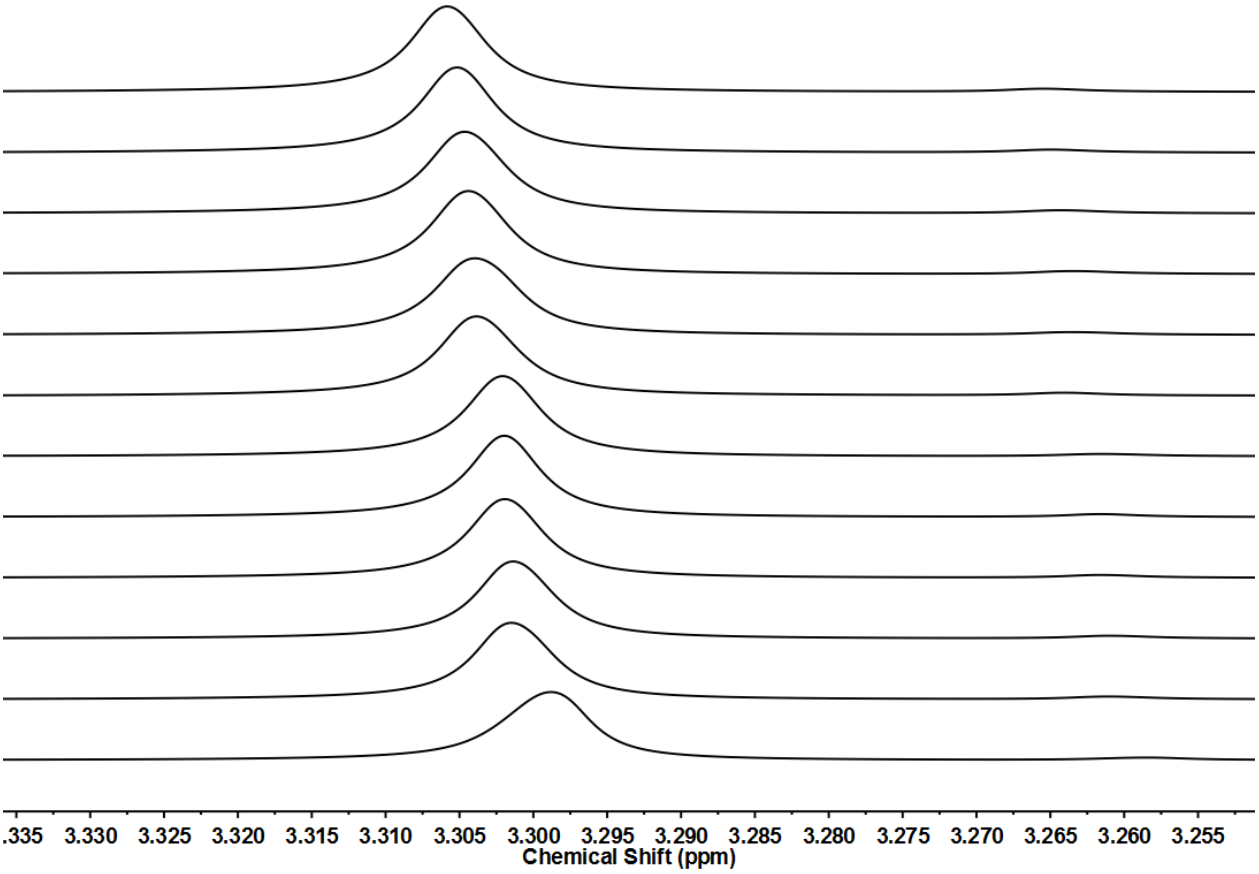

Figure 3. 16 The downfield shift of water peak in ^{1}H NMR titration in the presence of increasing CB[6] concentration.

3.2.4 PH TITRATION STUDIES

One aspect of interest in macrocylic host molecules is their potential in modifying the effective pKa (acid dissociation constant) values of included guest. The pKa value is highly dependent on the affinity of host towards protonated or deprotonated forms of guest and can result in desirable shift of its acidity constant [174]. Especially, CB has shown enhanced efficiency in changing the pKa values compared to Cyclodextrin hosts due to their higher binding affinity and selectivity. This strategy has been utilized effectively in fluorescent dye tuning [175], assaying [176], sensing [177] and drug delivery [178]. For instance, the host induced pKa change is reported to improve the efficiency of the drug in harshly gastric acidic environment and protects the drug from premature dimerization and decomposition [178]. Upon encapsulation, there is a shift in pKa value and stabilization of the protonated form of a molecule through ion dipole interaction as has been observed in benzimidazole based molecules. The pKa shift can be associated with both hydrophobic cavity and carbonyl rim of CB such that the hydrophobic cavity dislikes the ionic species whereas he carbonyl rim favors cationic guests which enhances the charge transfer of the encapsulated guest. Therefore, the acidity or basicity of the guest in CB cavity is predominantly determined by the host guest interaction. The shift in the acidity of a complex is in upward direction for weakly basic molecules as CB tends to act as a cation receptor while the opposite trend is expected for anion receptor host molecules [179].

Nic is a weak acid with an estimated pKa value of 5.6 due to the presence of phenol groups. At pH 7.4, the most stable species of Nic are in the deprontonated form [180]. Upon encapsulation of Nic in CB cavity the deprotonated species become more stable therefore decreasing the pKa value (Figure 3.17).

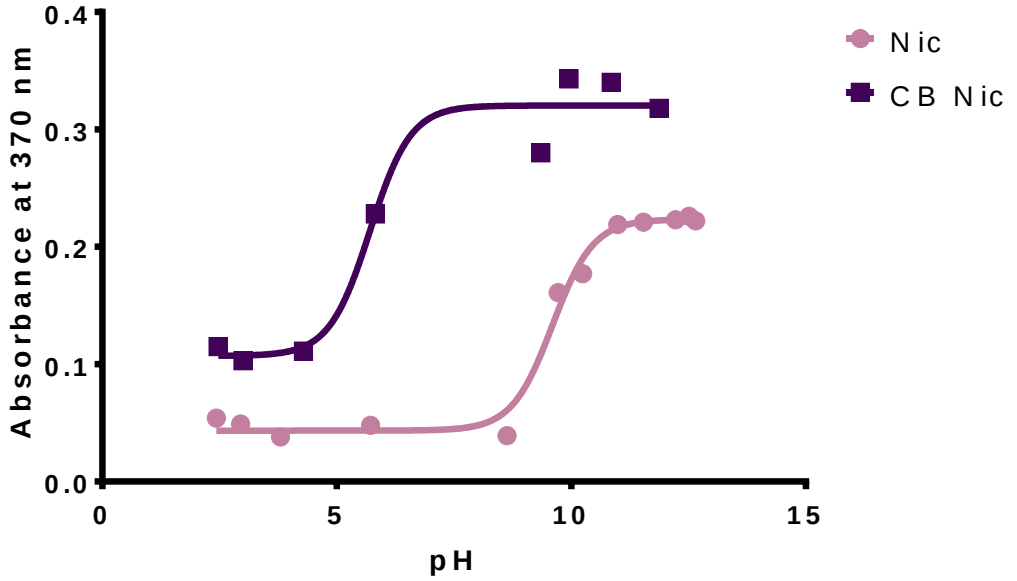

Figure 3. 17 UV-Vis absorbance of Nic at 370 nm at various pH in the absence and presence of CB[6].

3.2.5 CYCLIC VOLTAMMETRY

Various human diseases including different types of cancer are associated with redox imbalances and oxidative stress. It is well known that the ROS level varies in cancerous cells compared to the normal cells due to the accelerated metabolism. Redox modulating compounds exploits the present redox condition of the abnormal cells to their advantage as anti- cancer drug where they catalyze the oxidation of the redox- sensitive thiol- containing proteins and enzymes which will lead to cell apoptosis [181]. Nic is known to elevate the ROS level in Acute Myelogenous Leukemia Stem Cells without targeting the normal bone marrow [70]. Therefore, it is of interest to investigate the electrochemical behavior of Nic in the absence and in the presence of CB which would ultimately result in the de/modulation of biological activity.

In general, the Redox conversions on the guest and host usually lead to significant changes in the stability of the host and guest complex. Upon encapsulation, the negatively

charged carbonyl rim can potentially interact with positively charged species thereby, stabilizing the protonated form of a molecule through ion dipole interaction. The cyclic voltammogram of Nic in the absence and in the presence of increasing amount of CB is shown in Figure 3.18. The Redox behavior of Nic is quite well established in literature. It is evident that the nitro group in Nic is irreversibly reduced to N- phenylhydroxylamine during which four electrons/ proton transfer occurs [182]. The current diminished upon CB[6] inclusion which shows the smaller diffusion coefficient than the free Nic and stabilization of the guest molecule (Figure 3.18). On the other hand, though, the cathodic potentials peaks were supposed to move to more negative values due to the hindrance of electron transfer posed by CB[6] encapsulation. However, our observation does not follow the expected trend. This trial narrowly investigates the effect of Nic complexation and therefore future experiments are required to pave the path for future studies on the electrochemical behavior of the developed formulation for forthcoming *in vitro* and *in vivo* applications.

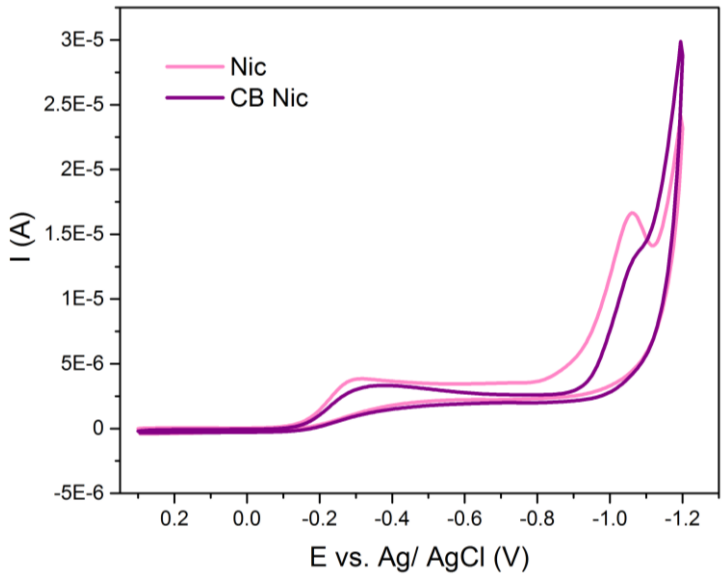

Figure 3. 18 The cylic voltagramm of Nic in the absence and presence of 3 equivalent of CB[6].

3.3 IN VITRO RELEASE STUDIES

The loading efficiency of CB[6], Nic was evaluated using the calibration curves. The loading efficiency was calculated to be 25±2%. Subsequently, the release of Nic fromCB[6] was determined under various conditions. To quantify the release at different time points, the calibration curve presented in Figure 3.19 was used where the absorbance at 339 nm was used to carry out the calculations. The release curve in aqueous media at room temperature and 37 ºC and aqueous media at pH 4.5 are shown in Figure 3.20a-c. The maximum percentage of drug release was observed to be around 5%. It was also seen that low pH did not exert favorable condition for the release of drug. The results suggest that aqueous media did not lead to significant release of drug. This results show the promise of the developed host guest complex for sequestering the drug as the cargo should not be released during systemic application and prior to reaching its target. However, as the MTT results rendered in the following chapter, the drug was efficiently released under *in vitro* condition leading to enhanced potency of the drug for both CB[6] Nic and CNP coated with CB[6].

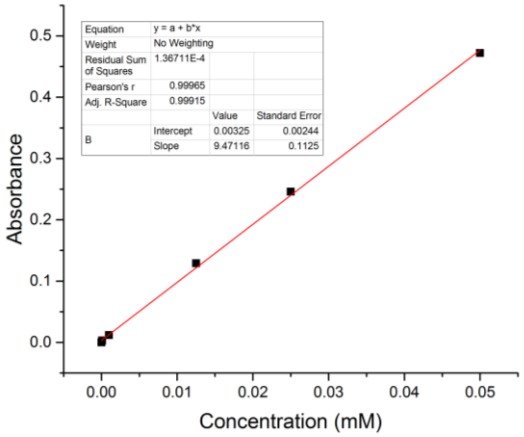

Figure 3. 19 The calibration curve used for determining the release profile.

The decreased release of the drug in low pH environment parallels with the pH titration observation where the shift in the titration curve was attributed to the stabilization of Nic in the presence of CB[6]. It should be mentioned that the kinetics studies were also attempted for CNP containing samples. However, the strong absorption of CNP along with the proximity of its peak to that of Nic hampered our quantification. Although, the results seem to be reasonable, further characterizations are under progress where we predict that the interference due to low solubility of Nic can be resolved. Furthermore, the release pattern should also be investigated in the presence of salt- containing environment which closely mimics the physiological conditions. This approach focuses on quantifying the bound drug instead of released drug.

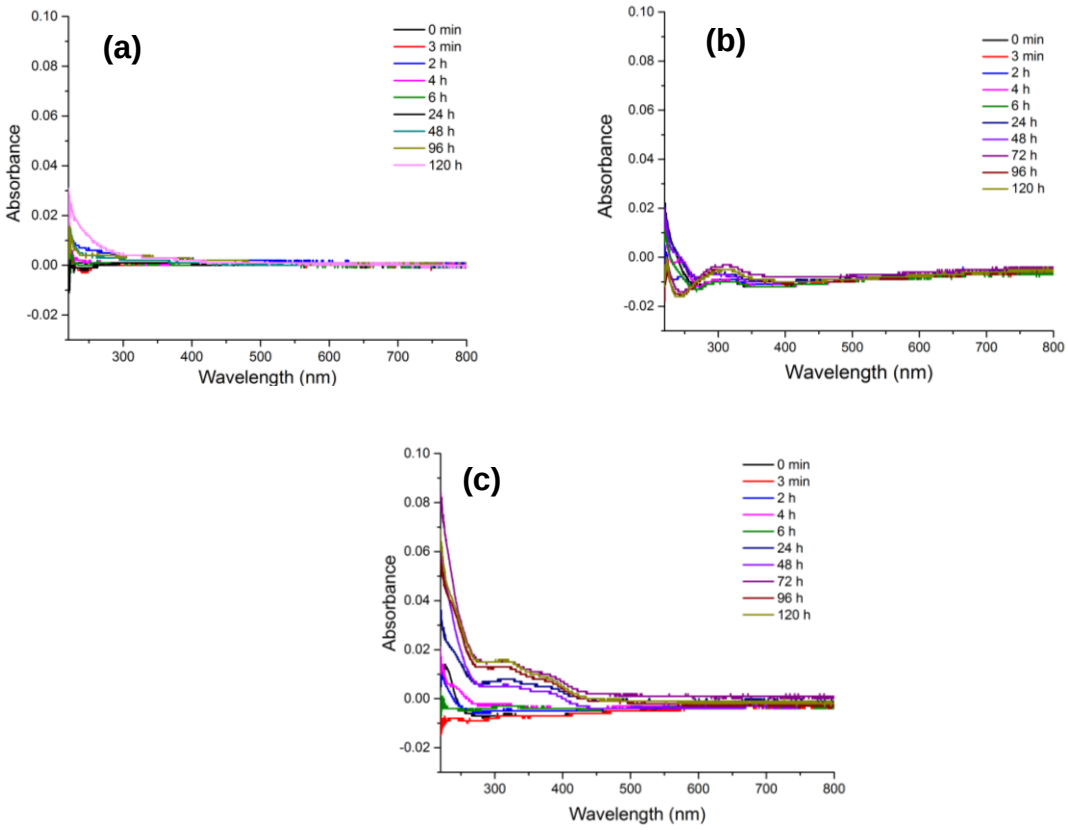

Figure 3. 20 The pattern of drug release for (a) aqueous media at room temperature (b) aqueous media at pH 4.5 at 37 ºC and (c) aqueous media at 37 ºC.

3.4 IN VITRO CELLULAR CYTOTOXICITY STUDIES

In order to evaluate the growth-inhibitory effect of CB[6]-CNP-Nic nanoparticles MTT assay was performed. Experiments were performed in estrogen receptor (ER) positive MCF-7 cell line. Bright field imaging of treated MCF-7 cells revealed the loss of cell growth density and cellular morphology selectively in population treated with (Figure 3.21c) Nic; (Figure 3.21h) CB[6]-CNP-Nic (post); (Figure 3.21i) CB[6]-CNP-Nic (pre) and (Figure 3.21e) CB[6]-Nic. On the other hand, (Figure 3.21b) CB[6]; (Figure 3.21d) CNP; (Figure 3.21f) CB[6]-CNP (post) and (Figure 3.21g) CB[6]-CNP (pre) did not change cell growth density and cellular morphology to any significant level compared to untreated MCF-7 cells (Figure 3.21a) itself. The MTT results showed that after 48 h incubation CNP, CB[6] and CB[6] CNP (post functionalized) did not induce any significant cytotoxic effect (Figure 3.j) for a range of used concentrations (from 1.5-50 μM) which is a crucial and encouraging characteristic as a drug delivery platform and future biological applications. The IC_{50} value of Nic, CB[6] Nic and CB[6] CNP Nic (post functionalized) was determined to be $(45\pm04)\times10^{-6}$ M, $(28\pm03)\times10^{-6}$ M and $(21\pm02)\times10^{-6}$ M, respectively (Figure 3.21k). The enhancement in the inhibitory effect of Nic in the presence of CB[6], emphasizes the facilitated Nic delivery using the host chemistry of CB[6] and the incorporation of CNP enhanced it further to improve host-guest interaction of CB[6] and CNP in reversible manner. It helps to incorporate and release Nic better in void of CB[6] during preparation of CB[6]-CNP when it is present on surface of CNP. This also can be attributed to the facile internalization and translocation inside the cell, sustained release of drug and enhanced bioavailability of Nic in CB[6] Nic and CB[6] CNP Nic formulations compared to the small molecule form of Nic, which is sparingly soluble in aqueous medium.

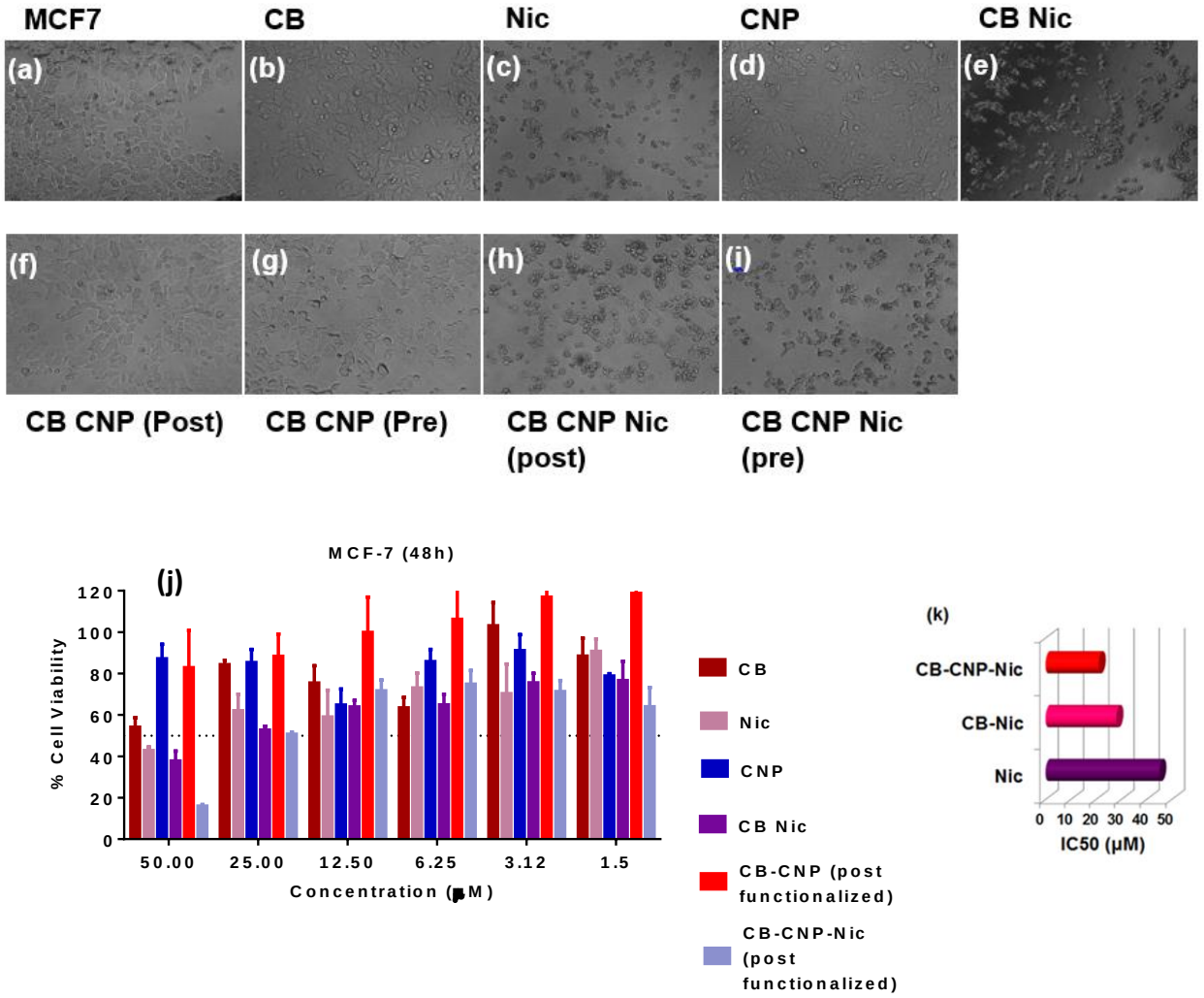

Figure 3. 21 Cell toxicity assay in MCF-7 cells. Bright field imaging (a-i) were performed on cells treated for 48h with 25 μM of Nic concentration in various formulations or equivalent of CNP, CB[6] and CB[6]-CNP (a-i). MTT assay was performed at Nic concentration ranging from 1.5 to 50 μM in various formulation form including CB[6]-Nic, Nic and CB[6]-CNP-Nic (post) while CB[6], CNP and CB[6]-CNP were used as positive control. (k) MTT results were used to calculate IC_{50} values for Nic formulations and compared to evaluate the improvement in cancer cell growth regression efficiency.

CHAPTER 4

CONCLUSION AND FUTURE OUTLOOK

4.1 CURRENT PERSPECTIVE

Herein, we reported on the successful synthesis of the novel carbon nanoparticles (CNP decorated with cucurbituril[6] (CB[6]) for the enhanced inhibition of cancer stem cells *via* targeting STAT3 pathway. The carbon nanoparticles were obtained from the environmentally benign hydrothermal synthetic route using Agave nectar as the carbohydrate precursor. The particles were either pre-functionalized or post-functionalized with CB[6] and were further loaded with STAT3 inhibitor Niclosamide (Nic). Comprehensive physiochemical characterization followed in order to confirm the successful synthesis of the novel nanoplatforms. Extensive studies including UV-Vis titration, 2D excitation- emission fluorescent titration, ^{1}H NMR titration, pH titration and cyclic voltammetry, FT-IR were carried out to confirm the interaction as well as to examine the stoichiometry and possible binding behavior of CB[6] and Nic. Finally, the potential of the developed nanoformulations were evaluated *in vitro* by examining the drug loading and release kinetics studies, monitoring size stability over one month in physiologically relevant media and assessing the cell viability in MCF-7 cell line by MTT assay.

The main findings can be summarized as follows:

- The hydrodynamic size of CNP, CNP post and pre coated with CB[6] were determined to be 76±13, 93±4 nm and 55±1 nm, respectively. On the other hand, the anhydrous size for post and pre coated samples was found to be 88±22 nm and 31±6 nm respectively. The average height was measured to be approximately nm for post and pre coated specimens.

- The hydrodynamic size remained virtually unchanged in the aqueous media at pH=7 and pH=4.5 and in aqueous sample containing 10% FBS over the course of one month suggesting the suitability of the developed particles for *in vitro* applications.

- The electrophoretic potential of the as synthesized CNP was circa -30 mV and varied depending on the chemical functionalization. However, the overall surface charge did not go beyond -18 mV, demonstrating the colloidal stability of the nanoparticles. This observation was compatible with the hydrodynamic stability of the particles.

- The UV-Vis spectroscopy revealed the interaction between CB[6],Nic and CNP coated Cb[6] with Nic.

- The presence of characteristic feature of CNP and CB[6] in the FTIR spectroscopy confirmed the success of synthetic strategy. Furthermore, through Raman spectroscopy the extent of surface functionalization was determined by tracking the intensity ratio of D and G band.

- The constructed Job's plot from tracking amide bond in FTIR revealed the 2:3 binding model.

- Titration studies by UV-Vis and fluorescent titration were hampered due to poor solubility and the strong scattering effects of CB[6]. Therefore, it did not yield conclusive parameters such as binding constant.

- The ^{1}H NMR titration studies elucidated the mechanism of interaction of CB[6] and Nic and provided useful information on the drug orientation and the portal of entry in CB[6] cavity.

- Drug loading capacity of CB and Nic was 25%. The kinetics of release of Nic was examined under various physiological media and it was shown that Nic is not significantly being released over extended period of time suggesting its suitability for release only at the site of interest as has been observed through *in vitro* cell studies.

- Approximately two fold enhancement in IC_{50} values were observed for the encapsulated drug vs free drug. The IC_{50} value of Nic, CB[6] Nic and CB[6] CNP Nic (post functionalized) was determined to be $(45\pm04)\times10^{-6}$ M, $(28\pm03)\times10^{-6}$ M and $(21\pm02)\times10^{-6}$ M, respectively. Hence, this novel nanoplatform holds the promise for sustained and enhanced chemotherapeutic delivery of sparingly soluble niclosamide for modulation of stem cell signaling pathways.

4.2 FUTURE OUTLOOK

In this thesis, the *in vitro* characterization has been carried out for confirming the enhanced efficacy of Nic in the presence of Nano-Carbobitaceae. Further *in vitro* test such as DNA fragmentation by propidium iodide staining followed by FACS analysis and gel electrophoresis are ongoing to further elucidate the potential of the formulation for inhibiting cancer cell growth. Through these studies, mechanisms underlying the cell apoptosis will be investigated. Furthermore, the successful delivery of Nic as the cargo is going to be traced by FT-IR and Raman imaging modalities. In addition, animal studies are currently under progress to demonstrate the potential of the nanoplatforms for drug delivery purposes *in vivo*.

As part of our future plan, the nanoparticles are going to be incorporated within bio-absorbable 3D printed esophageal stents for delivery of controlled doses of anti- neoplastic and/ or anti-inflammatory drug. The idea stems from the fact that the commercially available stents

come in narrow size options thus restricting their application. Therefore, towards "personalized stent" we will propose an translational engineering solution *via* the use of biodegradable shape memory polymers which directly targets the downsides of commercially available stents. The critical factor, though, is the choice of appropriate polymer matrix. In this case we propose the use of self-healing polymers which rivals its metallic base counterparts with the superiority of biodegradability. The polymer matrix is going to bear radio-opaque iodinated functionalities for accurate stent positioning guided through fluoroscopy. In our approach, another level of complexity is introduced and that is the sustained release of the anti- inflammatory drug from the polymeric matrix reservoir through a nanomedicine approach where we intend to combine the developed nano-carbobitace into our polymer for sustained release. Our multifunctional drug carrier is has also the potential of delivering controlled doses of anti- neoplastic therapeutics such as carboplatin, paclitaxel, cisplatin, fluorouracil. Most importantly, the architectural tuning of the polymer for personalized applications *via* 3D printing is going to be introduced for the first time. In this method, highly accurate, patient specific images of the esophagus and the tumor burden can be acquired by imaging modalities such as CT scanning and MRI. In the next step, 3D segmentation and visualization are going to be performed and a Computer-Aided Design (CAD) model of the segmented structures will begenerated. Ultimately, the proposed biodegradable shape memory polymer is printed layer by layer in an additive manufacturing scheme. Extensive materials and computational,and mechanical studies are to be conducted after the prototype development. Nevertheless, all the efforts would be meaningful only if the characterization of the system is made both in *vitro* and in *vivo* in a swine model guided by fluoroscopy.

The project has a high potential for preclinical/ clinical translation.

REFERENCES

[1] R.L. Siegel, K.D. Miller, A. Jemal, Cancer statistics, 2015, CA: a cancer journal for clinicians, 65 (2015) 5-29.

[2] L.N. Abdullah, E.K.-H. Chow, Mechanisms of chemoresistance in cancer stem cells, Clin Transl Med, 2 (2013) 3.

[3] A. Larochelle, J. Vormoor, H. Hanenberg, J.C. Wang, M. Bhatia, T. Lapidot, T. Moritz, B. Murdoch, X.L. Xiao, I. Kato, Identification of primitive human hematopoietic cells capable of repopulating NOD/SCID mouse bone marrow: implications for gene therapy, Nature medicine, 2 (1996) 1329-1337.

[4] D. Dick, Human acute myeloid leukemia is organized as a hierarchy that originates from a primitive hematopoietic cell, Nature Med, 3 (1997) 730-737.

[5] L.V. Nguyen, R. Vanner, P. Dirks, C.J. Eaves, Cancer stem cells: an evolving concept, Nature Reviews Cancer, 12 (2012) 133-143.

[6] A.W. Hamburger, S.E. Salmon, Primary bioassay of human tumor stem cells, Science, 197 (1977) 461-463.

[7] S.J. Morrison, J. Kimble, Asymmetric and symmetric stem-cell divisions in development and cancer, Nature, 441 (2006) 1068-1074.

[8] A. Singh, J. Settleman, EMT, cancer stem cells and drug resistance: an emerging axis of evil in the war on cancer, Oncogene, 29 (2010) 4741-4751.

[9] M. Al-Hajj, M.S. Wicha, A. Benito-Hernandez, S.J. Morrison, M.F. Clarke, Prospective identification of tumorigenic breast cancer cells, Proceedings of the National Academy of Sciences, 100 (2003) 3983-3988.

[10] L. Ricci-Vitiani, D.G. Lombardi, E. Pilozzi, M. Biffoni, M. Todaro, C. Peschle, R. De Maria, Identification and expansion of human colon-cancer-initiating cells, Nature, 445 (2007) 111-115.

[11] S.K. Singh, I.D. Clarke, M. Terasaki, V.E. Bonn, C. Hawkins, J. Squire, P.B. Dirks, Identification of a cancer stem cell in human brain tumors, Cancer research, 63 (2003) 5821-5828.

[12] M. Kim, H. Turnquist, J. Jackson, M. Sgagias, Y. Yan, M. Gong, M. Dean, J.G. Sharp, K. Cowan, The multidrug resistance transporter ABCG2 (breast cancer resistance protein 1) effluxes Hoechst 33342 and is overexpressed in hematopoietic stem cells, Clinical Cancer Research, 8 (2002) 22-28.

[13] C. Ginestier, M.H. Hur, E. Charafe-Jauffret, F. Monville, J. Dutcher, M. Brown, J. Jacquemier, P. Viens, C.G. Kleer, S. Liu, ALDH1 is a marker of normal and malignant human mammary stem cells and a predictor of poor clinical outcome, Cell stem cell, 1 (2007) 555-567.

[14] F. Nguyen-Khac, C. Lesty, V. Eclache, L. Couronné, O. Kosmider, J. Andrieux, M.A. Collonge-Rame, D. Penther, M. Lafage, C. Bilhou-Nabera, Chromosomal abnormalities in transformed Ph-negative myeloproliferative neoplasms are associated to the transformation subtype and independent of JAK2 and the TET2 mutations, Genes, Chromosomes and Cancer, 49 (2010) 919-927.

[15] P.C. Nowell, The clonal evolution of tumor cell populations, Science, 194 (1976) 23-28.

[16] J.E. Visvader, G.J. Lindeman, Cancer stem cells in solid tumours: accumulating evidence and unresolved questions, Nature Reviews Cancer, 8 (2008) 755-768.

[17] W.A. Woodward, E.P. Sulman, Cancer stem cells: markers or biomarkers?, Cancer and metastasis reviews, 27 (2008) 459-470.

[18] B. Beck, C. Blanpain, Unravelling cancer stem cell potential, Nature Reviews Cancer, 13 (2013) 727-738.

[19] S. Tabarestani, S. Ghafouri-Fard, Cancer stem cells and response to therapy, Asian Pacific Journal of Cancer Prevention, 13 (2012) 5947-5954.

[20] S. Hombach-Klonisch, S. Natarajan, T. Thanasupawat, M. Medapati, A. Pathak, S. Ghavami, T. Klonisch, Mechanisms of therapeutic resistance in cancer (stem) cells with emphasis on thyroid cancer cells, Frontiers in endocrinology, 5 (2014).

[21] M. Dean, ABC transporters, drug resistance, and cancer stem cells, Journal of mammary gland biology and neoplasia, 14 (2009) 3-9.

[22] M.J. Bissell, M.A. LaBarge, Context, tissue plasticity, and cancer: are tumor stem cells also regulated by the microenvironment?, Cancer cell, 7 (2005) 17-23.

[23] T. Borovski, E.M. Felipe De Sousa, L. Vermeulen, J.P. Medema, Cancer stem cell niche: the place to be, Cancer research, 71 (2011) 634-639.

[24] J. Voog, D.L. Jones, Stem cells and the niche: a dynamic duo, Cell stem cell, 6 (2010) 103-115.

[25] H. Korkaya, S. Liu, M.S. Wicha, Breast cancer stem cells, cytokine networks, and the tumor microenvironment, The Journal of clinical investigation, 121 (2011) 3804.

[26] V. Plaks, N. Kong, Z. Werb, The cancer stem cell niche: how essential is the niche in regulating stemness of tumor cells?, Cell stem cell, 16 (2015) 225-238.

[27] K. Polyak, R.A. Weinberg, Transitions between epithelial and mesenchymal states: acquisition of malignant and stem cell traits, Nature Reviews Cancer, 9 (2009) 265-273.

[28] S. Lamouille, J. Xu, R. Derynck, Molecular mechanisms of epithelial–mesenchymal transition, Nature reviews Molecular cell biology, 15 (2014) 178-196.

[29] D.S. Aaronson, C.M. Horvath, A road map for those who don't know JAK-STAT, Science, 296 (2002) 1653-1655.

[30] H. Yu, R. Jove, The STATs of cancer—new molecular targets come of age, Nature Reviews Cancer, 4 (2004) 97-105.

[31] T. Hirano, K. Ishihara, M. Hibi, Roles of STAT3 in mediating the cell growth, differentiation and survival signals relayed through the IL-6 family of cytokine receptors, Oncogene, 19 (2000) 2548-2556.

[32] O. Dreesen, A.H. Brivanlou, Signaling pathways in cancer and embryonic stem cells, Stem cell reviews, 3 (2007) 7-17.

[33] J.E. Darnell, Transcription factors as targets for cancer therapy, Nature Reviews Cancer, 2 (2002) 740-749.

[34] H. Yu, H. Lee, A. Herrmann, R. Buettner, R. Jove, Revisiting STAT3 signalling in cancer: new and unexpected biological functions, Nature reviews Cancer, 14 (2014) 736-746.

[35] P.A. Furth, R.E. Nakles, S. Millman, E.S. Diaz-Cruz, M.C. Cabrera, Signal transducer and activator of transcription 5 as a key signaling pathway in normal mammary gland developmental biology and breast cancer, Breast Cancer Res, 13 (2011) 220.

[36] L. Song, J. Turkson, J.G. Karras, R. Jove, E.B. Haura, Activation of Stat3 by receptor tyrosine kinases and cytokines regulates survival in human non-small cell carcinoma cells, Oncogene, 22 (2003) 4150-4165.

[37] R. Catlett-Falcone, T.H. Landowski, M.M. Oshiro, J. Turkson, A. Levitzki, R. Savino, G. Ciliberto, L. Moscinski, J.L. Fernández-Luna, G. Nuñez, Constitutive activation of Stat3 signaling confers resistance to apoptosis in human U266 myeloma cells, Immunity, 10 (1999) 105-115.

[38] N. Kiuchi, K. Nakajima, M. Ichiba, T. Fukada, M. Narimatsu, K. Mizuno, M. Hibi, T. Hirano, STAT3 is required for the gp130-mediated full activation of the c-myc gene, The Journal of experimental medicine, 189 (1999) 63-73.

[39] J.F. Bromberg, M.H. Wrzeszczynska, G. Devgan, Y. Zhao, R.G. Pestell, C. Albanese, J.E. Darnell, Stat3 as an oncogene, Cell, 98 (1999) 295-303.

[40] N. Kanda, H. Seno, Y. Konda, H. Marusawa, M. Kanai, T. Nakajima, T. Kawashima, A. Nanakin, T. Sawabu, Y. Uenoyama, STAT3 is constitutively activated and supports cell survival in association with survivin expression in gastric cancer cells, Oncogene, 23 (2004) 4921-4929.

[41] S.S. Chung, N. Giehl, Y. Wu, J.V. Vadgama, STAT3 activation in HER2-overexpressing breast cancer promotes epithelial-mesenchymal transition and cancer stem cell traits, International journal of oncology, 44 (2014) 403-411.

[42] B.D. Looyenga, D. Hutchings, I. Cherni, C. Kingsley, G.J. Weiss, J.P. MacKeigan, STAT3 is activated by JAK2 independent of key oncogenic driver mutations in non-small cell lung carcinoma, PloS one, 7 (2012) e30820.

[43] L. Lin, J. Fuchs, C. Li, V. Olson, T. Bekaii-Saab, J. Lin, STAT3 signaling pathway is necessary for cell survival and tumorsphere forming capacity in ALDH+/CD133+ stem cell-like human colon cancer cells, Biochemical and biophysical research communications, 416 (2011) 246-251.

[44] Y. Zhang, X.L. Du, C.J. Wang, D.C. Lin, X. Ruan, Y.B. Feng, Y.Q. Huo, H. Peng, J.L. Cui, T.T. Zhang, Reciprocal activation between PLK1 and Stat3 contributes to survival and proliferation of esophageal cancer cells, Gastroenterology, 142 (2012) 521-530. e523.

[45] C.L. Campbell, Z. Jiang, D.M. Savarese, T.M. Savarese, Increased expression of the interleukin-11 receptor and evidence of STAT3 activation in prostate carcinoma, The American journal of pathology, 158 (2001) 25-32.

[46] R.-J. Chen, Y.-S. Ho, H.-R. Guo, Y.-J. Wang, Rapid activation of Stat3 and ERK1/2 by nicotine modulates cell proliferation in human bladder cancer cells, Toxicological Sciences, 104 (2008) 283-293.

[47] B.E. Barton, J.G. Karras, T.F. Murphy, A. Barton, H.F. Huang, Signal transducer and activator of transcription 3 (STAT3) activation in prostate cancer: Direct STAT3 inhibition induces apoptosis in prostate cancer lines, Molecular cancer therapeutics, 3 (2004) 11-20.

[48] A. Subramaniam, M.K. Shanmugam, E. Perumal, F. Li, A. Nachiyappan, X. Dai, S.N. Swamy, K.S. Ahn, A.P. Kumar, B.K. Tan, Potential role of signal transducer and activator of transcription (STAT) 3 signaling pathway in inflammation, survival, proliferation and invasion of hepatocellular carcinoma, Biochimica et Biophysica Acta (BBA)-Reviews on Cancer, 1835 (2013) 46-60.

[49] J. Zhou, J. Wulfkuhle, H. Zhang, P. Gu, Y. Yang, J. Deng, J.B. Margolick, L.A. Liotta, E. Petricoin, Y. Zhang, Activation of the PTEN/mTOR/STAT3 pathway in breast cancer stem-like cells is required for viability and maintenance, Proceedings of the National Academy of Sciences, 104 (2007) 16158-16163.

[50] L. Lin, R. Amin, G. Gallicano, E. Glasgow, W. Jogunoori, J. Jessup, M. Zasloff, J. Marshall, K. Shetty, L. Johnson, The STAT3 inhibitor NSC 74859 is effective in hepatocellular cancers with disrupted TGF-β signaling, Oncogene, 28 (2009) 961-972.

[51] M.M. Sherry, A. Reeves, J.K. Wu, B.H. Cochran, STAT3 is required for proliferation and maintenance of multipotency in glioblastoma stem cells, Stem cells, 27 (2009) 2383-2392.

[52] C.P. Gibbs, V.G. Kukekov, J.D. Reith, O. Tchigrinova, O.N. Suslov, E.W. Scott, S.C. Ghivizzani, T.N. Ignatova, D.A. Steindler, Stem-like cells in bone sarcomas: implications for tumorigenesis, Neoplasia, 7 (2005) 967-976.

[53] H. Yu, M. Kortylewski, D. Pardoll, Crosstalk between cancer and immune cells: role of STAT3 in the tumour microenvironment, Nature Reviews Immunology, 7 (2007) 41-51.

[54] X. Wang, P.J. Crowe, D. Goldstein, J.-L. Yang, STAT3 inhibition, a novel approach to enhancing targeted therapy in human cancers (review), International journal of oncology, 41 (2012) 1181-1191.

[55] A. Jarnicki, T. Putoczki, M. Ernst, Review Stat3: linking inflammation to epithelial cancer-more than a" gut" feeling?, (2010).

[56] X. Ren, L. Duan, Q. He, Z. Zhang, Y. Zhou, D. Wu, J. Pan, D. Pei, K. Ding, Identification of niclosamide as a new small-molecule inhibitor of the STAT3 signaling pathway, ACS medicinal chemistry letters, 1 (2010) 454-459.

[57] P. Andrews, J. Thyssen, D. Lorke, The biology and toxicology of molluscicides, Bayluscide, Pharmacology & therapeutics, 19 (1982) 245-295.

[58] B.M. Al-Hadiya, Niclosamide: comprehensive profile, Profiles of Drug Substances, Excipients and Related Methodology, 32 (2005) 67-96.

[59] Y. Li, P.-K. Li, M.J. Roberts, R.C. Arend, R.S. Samant, D.J. Buchsbaum, Multi-targeted therapy of cancer by niclosamide: A new application for an old drug, Cancer letters, 349 (2014) 8-14.

[60] P. Coura-Filho, N.M. Mendes, C.P.d. Souza, J.P. Pereira, The prolonged use of niclosamide as a molluscicide for the control of Schistosoma mansoni, Revista do Instituto de Medicina Tropical de São Paulo, 34 (1992) 427-431.

[61] C.-J. Wu, J.-T. Jan, C.-M. Chen, H.-P. Hsieh, D.-R. Hwang, H.-W. Liu, C.-Y. Liu, H.-W. Huang, S.-C. Chen, C.-F. Hong, Inhibition of severe acute respiratory syndrome coronavirus replication by niclosamide, Antimicrobial agents and chemotherapy, 48 (2004) 2693-2696.

[62] S.C. Gupta, B. Sung, S. Prasad, L.J. Webb, B.B. Aggarwal, Cancer drug discovery by repurposing: teaching new tricks to old dogs, Trends in pharmacological sciences, 34 (2013) 508-517.

[63] M.S. Lipsky, L.K. Sharp, From idea to market: the drug approval process, The Journal of the American Board of Family Practice, 14 (2001) 362-367.

[64] S.M. Strittmatter, Overcoming drug development bottlenecks with repurposing: old drugs learn new tricks, Nature medicine, 20 (2014) 590-591.

[65] M. Chen, J. Wang, J. Lu, M.C. Bond, X.-R. Ren, H.K. Lyerly, L.S. Barak, W. Chen, The anti-helminthic niclosamide inhibits Wnt/Frizzled1 signaling, Biochemistry, 48 (2009) 10267-10274.

[66] W. Lu, C. Lin, M.J. Roberts, W.R. Waud, G.A. Piazza, Y. Li, Niclosamide suppresses cancer cell growth by inducing Wnt co-receptor LRP6 degradation and inhibiting the Wnt/beta-catenin pathway, PloS one, 6 (2011) e29290.

[67] A.D. Balgi, B.D. Fonseca, E. Donohue, T. Tsang, P. Lajoie, C.G. Proud, I.R. Nabi, M. Roberge, Screen for chemical modulators of autophagy reveals novel therapeutic inhibitors of mTORC1 signaling, PLoS One, 4 (2009) e7124.

[68] R. Li, Z. Hu, S.-Y. Sun, Z.G. Chen, T.K. Owonikoko, G.L. Sica, S.S. Ramalingam, W.J. Curran, F.R. Khuri, X. Deng, Niclosamide overcomes acquired resistance to erlotinib through suppression of STAT3 in non–small cell lung cancer, Molecular cancer therapeutics, 12 (2013) 2200-2212.

[69] S. You, R. Li, D. Park, M. Xie, G.L. Sica, Y. Cao, Z.-Q. Xiao, X. Deng, Disruption of STAT3 by niclosamide reverses radioresistance of human lung cancer, Molecular cancer therapeutics, 13 (2014) 606-616.

[70] Y. Jin, Z. Lu, K. Ding, J. Li, X. Du, C. Chen, X. Sun, Y. Wu, J. Zhou, J. Pan, Antineoplastic mechanisms of niclosamide in acute myelogenous leukemia stem cells: inactivation of the NF-κB pathway and generation of reactive oxygen species, Cancer research, 70 (2010) 2516-2527.

[71] A.M. Wang, H.H. Ku, Y.C. Liang, Y.C. Chen, Y.M. Hwu, T.S. Yeh, The autonomous notch signal pathway is activated by baicalin and baicalein but is suppressed by niclosamide in K562 cells, Journal of cellular biochemistry, 106 (2009) 682-692.

[72] Y.-C. Wang, T.-K. Chao, C.-C. Chang, Y.-T. Yo, M.-H. Yu, H.-C. Lai, Drug screening identifies niclosamide as an inhibitor of breast cancer stem-like cells, PloS one, 8 (2013) e74538.

[73] Y.-T. Yo, Y.-W. Lin, Y.-C. Wang, C. Balch, R.-L. Huang, M.W. Chan, H.-K. Sytwu, C.-K. Chen, C.-C. Chang, K.P. Nephew, Growth Inhibition of Ovarian Tumor–Initiating Cells by Niclosamide, Molecular cancer therapeutics, 11 (2012) 1703-1712.

[74] S.-Y. Kim, J.W. Kang, X. Song, B.K. Kim, Y.D. Yoo, Y.T. Kwon, Y.J. Lee, Role of the IL-6-JAK1-STAT3-Oct-4 pathway in the conversion of non-stem cancer cells into cancer stem-like cells, Cellular signalling, 25 (2013) 961-969.

[75] R. Li, S. You, Z. Hu, Z.G. Chen, G.L. Sica, F.R. Khuri, W.J. Curran, D.M. Shin, X. Deng, Inhibition of STAT3 by niclosamide synergizes with erlotinib against head and neck cancer, PloS one, 8 (2013).

[76] Y. Chang, T. Yeh, K. Lin, W. Chen, H. Yao, S. Lan, Y. Wu, H. Hsieh, C. Chen, C. Chen, Pharmacokinetics of anti-SARS-CoV agent niclosamide and its analogs in rats, Journal of Food and Drug Analysis, 14 (2006) 329.

[77] B. Devarakonda, R.A. Hill, W. Liebenberg, M. Brits, M.M. de Villiers, Comparison of the aqueous solubilization of practically insoluble niclosamide by polyamidoamine (PAMAM) dendrimers and cyclodextrins, International journal of pharmaceutics, 304 (2005) 193-209.

[78] M.-Y. Heo, Z.-Z. Piao, T.-W. Kim, Q.-R. Cao, A. Kim, B.-J. Lee, Effect of solubilizing and microemulsifying excipients in polyethylene glycol 6000 solid dispersion on enhanced dissolution and bioavailability of ketoconazole, Archives of pharmacal research, 28 (2005) 604-611.

[79] S.K. Misra, T.W. Jensen, D. Pan, Enriched inhibition of cancer and stem-like cancer cells via STAT-3 modulating niclocelles, Nanoscale, 7 (2015) 7127-7132.

[80] J.W. Steed, J.L. Atwood, Supramolecular chemistry, John Wiley & Sons, 2013.

[81] H. Dodziuk, Introduction to supramolecular chemistry, Springer Science & Business Media, 2002.

[82] A. Villiers, Sur la fermentation de la fécule par l'action du ferment butyrique, Compt. Rend. Acad. Sci, 112 (1891) 536-538.

[83] C.D. Gutsche, Calixarenes: an introduction, Royal Society of Chemistry, 2008.

[84] T. Ogoshi, S. Kanai, S. Fujinami, T.-a. Yamagishi, Y. Nakamoto, para-Bridged symmetrical pillar [5] arenes: their Lewis acid catalyzed synthesis and host–guest property, Journal of the American Chemical Society, 130 (2008) 5022-5023.

[85] R. Behrend, E. Meyer, F. Rusche, I. Ueber Condensationsproducte aus Glycoluril und Formaldehyd, Justus Liebigs Annalen der Chemie, 339 (1905) 1-37.

[86] M.S. Lah, V.L. Pecoraro, Isolation and characterization of {MnII [MnIII (salicylhydroximate)] 4 (acetate) 2 (DMF) 6}. cntdot. 2DMF: an inorganic analog of M2+ (12-crown-4), Journal of the American Chemical Society, 111 (1989) 7258-7259.

[87] C.J. Pedersen, Cyclic polyethers and their complexes with metal salts, Journal of the American Chemical Society, 89 (1967) 7017-7036.

[88] J. Gabard, A. Collet, Synthesis of a (D 3)-bis (cyclotriveratrylenyl) macrocage by stereospecific replication of a (C 3)-subunit, Journal of the Chemical Society, Chemical Communications, (1981) 1137-1139.

[89] H.-J. Buschmann, A. Wego, E. Schollmeyer, D. Döpp, Synthesis of Cucurbituril-spermine-[2] rotaxanes of the Amide-type, Supramolecular Chemistry, 11 (2000) 225-231.

[90] J.-P. Desvergne, H. Bouas-Laurent, Cation complexing photochromic materials involving bisanthracenes linked by a polyether chain. Preparation of a crown-ether by photocycloisomerization, Journal of the Chemical Society, Chemical Communications, (1978) 403-404.

[91] Y. Zhou, H. Li, Y.-W. Yang, Controlled drug delivery systems based on calixarenes, Chinese Chemical Letters, (2015).

[92] S. Walker, R. Oun, F.J. McInnes, N.J. Wheate, The potential of cucurbit [n] urils in drug delivery, Israel Journal of Chemistry, 51 (2011) 616-624.

[93] J.L. Bolliger, A.M. Belenguer, J.R. Nitschke, Enantiopure Water-Soluble [Fe4L6] Cages: Host–Guest Chemistry and Catalytic Activity, Angewandte Chemie International Edition, 52 (2013) 7958-7962.

[94] B.C. Pemberton, R. Raghunathan, S. Volla, J. Sivaguru, From containers to catalysts: supramolecular catalysis within cucurbiturils, Chemistry-A European Journal, 18 (2012) 12178-12190.

[95] N. Barooah, J. Mohanty, H. Pal, A.C. Bhasikuttan, Stimulus-responsive supramolecular p K a tuning of cucurbit [7] uril encapsulated coumarin 6 dye, The Journal of Physical Chemistry B, 116 (2012) 3683-3689.

[96] A.L. Koner, W.M. Nau, Cucurbituril encapsulation of fluorescent dyes, Supramolecular Chemistry, 19 (2007) 55-66.

[97] C.P. Carvalho, A. Norouzy, V. Ribeiro, W.M. Nau, U. Pischel, Cucurbiturils as supramolecular inhibitors of DNA restriction by type II endonucleases, Organic & biomolecular chemistry, 13 (2015) 2866-2869.

[98] D.T. Dang, H.D. Nguyen, M. Merkx, L. Brunsveld, Supramolecular Control of Enzyme Activity through Cucurbit [8] uril-Mediated Dimerization, Angewandte Chemie, 125 (2013) 2987-2991.

[99] W. Freeman, W. Mock, N. Shih, Cucurbituril, Journal of the American Chemical Society, 103 (1981) 7367-7368.

[100] E. Masson, X. Ling, R. Joseph, L. Kyeremeh-Mensah, X. Lu, Cucurbituril chemistry: a tale of supramolecular success, Rsc Advances, 2 (2012) 1213-1247.

[101] L. Cao, M. Šekutor, P.Y. Zavalij, K. Mlinarić-Majerski, R. Glaser, L. Isaacs, Cucurbit [7] uril· Guest Pair with an Attomolar Dissociation Constant, Angewandte Chemie International Edition, 53 (2014) 988-993.

[102] E. Shchepotina, E. Pashkina, E. Yakushenko, V. Kozlov, Cucurbiturils as containers for medicinal compounds, Nanotechnologies in Russia, 6 (2011) 773-779.

[103] N. Saleh, I. Ghosh, W.M. Nau, Cucurbituril in drug delivery and for biomedi-cal applications, RSC Publishing: Cambridge, UK, 2013.

[104] V.D. Uzunova, C. Cullinane, K. Brix, W.M. Nau, A.I. Day, Toxicity of cucurbit [7] uril and cucurbit [8] uril: an exploratory in vitro and in vivo study, Organic & biomolecular chemistry, 8 (2010) 2037-2042.

[105] G. Hettiarachchi, D. Nguyen, J. Wu, D. Lucas, D. Ma, L. Isaacs, V. Briken, Toxicology and drug delivery by cucurbit [n] uril type molecular containers, PLoS One, 5 (2010) e10514.

[106] C.J. Porter, N.L. Trevaskis, W.N. Charman, Lipids and lipid-based formulations: optimizing the oral delivery of lipophilic drugs, Nature Reviews Drug Discovery, 6 (2007) 231-248.

[107] C.A. Lipinski, Drug-like properties and the causes of poor solubility and poor permeability, Journal of pharmacological and toxicological methods, 44 (2000) 235-249.

[108] A.L. Koner, I. Ghosh, N.i. Saleh, W.M. Nau, Supramolecular encapsulation of benzimidazole-derived drugs by cucurbit [7] uril, Canadian Journal of Chemistry, 89 (2011) 139-147.

[109] D. Ma, G. Hettiarachchi, D. Nguyen, B. Zhang, J.B. Wittenberg, P.Y. Zavalij, V. Briken, L. Isaacs, Acyclic cucurbit [n] uril molecular containers enhance the solubility and bioactivity of poorly soluble pharmaceuticals, Nature Chemistry, 4 (2012) 503-510.

[110] N.i. Saleh, A. Khaleel, H. Al-Dmour, B. al-Hindawi, E. Yakushenko, Host–guest complexes of cucurbit [7] uril with albendazole in solid state, Journal of thermal analysis and calorimetry, 111 (2013) 385-392.

[111] J.A. Plumb, B. Venugopal, R. Oun, N. Gomez-Roman, Y. Kawazoe, N.S. Venkataramanan, N.J. Wheate, Cucurbit [7] uril encapsulated cisplatin overcomes cisplatin resistance via a pharmacokinetic effect, Metallomics, 4 (2012) 561-567.

[112] N.J. Wheate, D.P. Buck, A.I. Day, J.G. Collins, Cucurbit [n] uril binding of platinum anticancer complexes, Dalton Transactions, (2006) 451-458.

[113] Y. Zhao, M.S. Bali, C. Cullinane, A.I. Day, J.G. Collins, Synthesis, cytotoxicity and cucurbituril binding of triamine linked dinuclear platinum complexes, Dalton Transactions, (2009) 5190-5198.

[114] K.I. Assaf, W.M. Nau, Cucurbiturils: from synthesis to high-affinity binding and catalysis, Chemical Society Reviews, 44 (2015) 394-418.

[115] S. Iijima, Helical microtubules of graphitic carbon, nature, 354 (1991) 56-58.

[116] K.S. Novoselov, A.K. Geim, S. Morozov, D. Jiang, Y. Zhang, S.a. Dubonos, I. Grigorieva, A. Firsov, Electric field effect in atomically thin carbon films, science, 306 (2004) 666-669.

[117] S.w. Mitura, Nucleation of diamond powder particles in an RF methane plasma, Journal of Crystal Growth, 80 (1987) 417-424.

[118] H. Li, Z. Kang, Y. Liu, S.-T. Lee, Carbon nanodots: synthesis, properties and applications, Journal of materials chemistry, 22 (2012) 24230-24253.

[119] T.C. Fitzgibbons, M. Guthrie, E.-s. Xu, V.H. Crespi, S.K. Davidowski, G.D. Cody, N. Alem, J.V. Badding, Benzene-derived carbon nanothreads, Nature materials, (2014).

[120] K. Hola, Y. Zhang, Y. Wang, E.P. Giannelis, R. Zboril, A.L. Rogach, Carbon dots—Emerging light emitters for bioimaging, cancer therapy and optoelectronics, Nano Today, 9 (2014) 590-603.

[121] X. Xu, R. Ray, Y. Gu, H.J. Ploehn, L. Gearheart, K. Raker, W.A. Scrivens, Electrophoretic analysis and purification of fluorescent single-walled carbon nanotube fragments, Journal of the American Chemical Society, 126 (2004) 12736-12737.

[122] Y.-P. Sun, B. Zhou, Y. Lin, W. Wang, K.S. Fernando, P. Pathak, M.J. Meziani, B.A. Harruff, X. Wang, H. Wang, Quantum-sized carbon dots for bright and colorful photoluminescence, Journal of the American Chemical Society, 128 (2006) 7756-7757.

[123] X. Zhai, P. Zhang, C. Liu, T. Bai, W. Li, L. Dai, W. Liu, Highly luminescent carbon nanodots by microwave-assisted pyrolysis, Chem. Commun., 48 (2012) 7955-7957.

[124] S. Liu, J. Tian, L. Wang, Y. Zhang, X. Qin, Y. Luo, A.M. Asiri, A.O. Al-Youbi, X. Sun, Hydrothermal Treatment of Grass: A Low-Cost, Green Route to Nitrogen-Doped, Carbon-Rich, Photoluminescent Polymer Nanodots as an Effective Fluorescent Sensing Platform for Label-Free Detection of Cu (II) Ions, Advanced Materials, 24 (2012) 2037-2041.

[125] Q.-L. Zhao, Z.-L. Zhang, B.-H. Huang, J. Peng, M. Zhang, D.-W. Pang, Facile preparation of low cytotoxicity fluorescent carbon nanocrystals by electrooxidation of graphite, Chem. Commun., (2008) 5116-5118.

[126] H. Zhu, X. Wang, Y. Li, Z. Wang, F. Yang, X. Yang, Microwave synthesis of fluorescent carbon nanoparticles with electrochemiluminescence properties, Chemical Communications, (2009) 5118-5120.

[127] X. Wang, K. Qu, B. Xu, J. Ren, X. Qu, Microwave assisted one-step green synthesis of cell-permeable multicolor photoluminescent carbon dots without surface passivation reagents, Journal of Materials Chemistry, 21 (2011) 2445-2450.

[128] S. Sahu, B. Behera, T.K. Maiti, S. Mohapatra, Simple one-step synthesis of highly luminescent carbon dots from orange juice: application as excellent bio-imaging agents, Chemical Communications, 48 (2012) 8835-8837.

[129] B. De, N. Karak, A green and facile approach for the synthesis of water soluble fluorescent carbon dots from banana juice, Rsc Advances, 3 (2013) 8286-8290.

[130] A. Konwar, N. Gogoi, G. Majumdar, D. Chowdhury, Green chitosan–carbon dots nanocomposite hydrogel film with superior properties, Carbohydrate polymers, 115 (2015) 238-245.

[131] M.P. Sk, A. Jaiswal, A. Paul, S.S. Ghosh, A. Chattopadhyay, Presence of amorphous carbon nanoparticles in food caramels, Scientific reports, 2 (2012).

[132] C. Jiang, H. Wu, X. Song, X. Ma, J. Wang, M. Tan, Presence of photoluminescent carbon dots in Nescafe® original instant coffee: Applications to bioimaging, Talanta, 127 (2014) 68-74.

[133] B. Das, P. Dadhich, P. Pal, P.K. Srivas, K. Bankoti, S. Dhara, Carbon nanodots from date molasses: new nanolights for the in vitro scavenging of reactive oxygen species, Journal of Materials Chemistry B, 2 (2014) 6839-6847.

[134] L. Wu, M. Luderer, X. Yang, C. Swain, H. Zhang, K. Nelson, A.J. Stacy, B. Shen, G.M. Lanza, D. Pan, Surface passivation of carbon nanoparticles with branched macromolecules influences near infrared bioimaging, Theranostics, 3 (2013) 677.

[135] S.Y. Lim, W. Shen, Z. Gao, Carbon quantum dots and their applications, Chemical Society Reviews, 44 (2015) 362-381.

[136] W. Wei, C. Xu, L. Wu, J. Wang, J. Ren, X. Qu, Non-enzymatic-browning-reaction: a versatile route for production of nitrogen-doped carbon dots with tunable multicolor luminescent display, Scientific reports, 4 (2014).

[137] G. Hong, S. Diao, A.L. Antaris, H. Dai, Carbon Nanomaterials for Biological Imaging and Nanomedicinal Therapy, Chemical reviews, (2015).

[138] S.-T. Yang, L. Cao, P.G. Luo, F. Lu, X. Wang, H. Wang, M.J. Meziani, Y. Liu, G. Qi, Y.-P. Sun, Carbon dots for optical imaging in vivo, Journal of the American Chemical Society, 131 (2009) 11308-11309.

[139] P. Mukherjee, S.K. Misra, M.C. Gryka, H.H. Chang, S. Tiwari, W.L. Wilson, J.W. Scott, R. Bhargava, D. Pan, Tunable Luminescent Carbon Nanospheres with Well-Defined Nanoscale Chemistry for Synchronized Imaging and Therapy, Small, (2015).

[140] L. Wu, X. Cai, K. Nelson, W. Xing, J. Xia, R. Zhang, A.J. Stacy, M. Luderer, G.M. Lanza, L.V. Wang, A green synthesis of carbon nanoparticles from honey and their use in real-time photoacoustic imaging, Nano research, 6 (2013) 312-325.

[141] P. Huang, J. Lin, X. Wang, Z. Wang, C. Zhang, M. He, K. Wang, F. Chen, Z. Li, G. Shen, Light-triggered theranostics based on photosensitizer-conjugated carbon dots for simultaneous enhanced-fluorescence imaging and photodynamic therapy, Advanced Materials, 24 (2012) 5104-5110.

[142] L. Cao, X. Wang, M.J. Meziani, F. Lu, H. Wang, P.G. Luo, Y. Lin, B.A. Harruff, L.M. Veca, D. Murray, Carbon dots for multiphoton bioimaging, Journal of the American Chemical Society, 129 (2007) 11318-11319.

[143] P.-C. Hsu, Z.-Y. Shih, C.-H. Lee, H.-T. Chang, Synthesis and analytical applications of photoluminescent carbon nanodots, Green Chemistry, 14 (2012) 917-920.

[144] D. Pan, M. Pramanik, A. Senpan, J.S. Allen, H. Zhang, S.A. Wickline, L.V. Wang, G.M. Lanza, Molecular photoacoustic imaging of angiogenesis with integrin-targeted gold nanobeacons, The FASEB Journal, 25 (2011) 875-882.

[145] P.G. Luo, S. Sahu, S.-T. Yang, S.K. Sonkar, J. Wang, H. Wang, G.E. LeCroy, L. Cao, Y.-P. Sun, Carbon "quantum" dots for optical bioimaging, Journal of Materials Chemistry B, 1 (2013) 2116-2127.

[146] J.C.G. Esteves da Silva, H.M.R. Gonçalves, Analytical and bioanalytical applications of carbon dots, TrAC Trends in Analytical Chemistry, 30 (2011) 1327-1336.

[147] Y. Song, D. Feng, W. Shi, X. Li, H. Ma, Parallel comparative studies on the toxic effects of unmodified CdTe quantum dots, gold nanoparticles, and carbon nanodots on live cells as well as green gram sprouts, Talanta, 116 (2013) 237-244.

[148] S. Ray, A. Saha, N.R. Jana, R. Sarkar, Fluorescent carbon nanoparticles: synthesis, characterization, and bioimaging application, The Journal of Physical Chemistry C, 113 (2009) 18546-18551.

[149] S.-T. Yang, X. Wang, H. Wang, F. Lu, P.G. Luo, L. Cao, M.J. Meziani, J.-H. Liu, Y. Liu, M. Chen, Carbon dots as nontoxic and high-performance fluorescence imaging agents, The Journal of Physical Chemistry C, 113 (2009) 18110-18114.

[150] X. Huang, F. Zhang, L. Zhu, K.Y. Choi, N. Guo, J. Guo, K. Tackett, P. Anilkumar, G. Liu, Q. Quan, Effect of injection routes on the biodistribution, clearance, and tumor uptake of carbon dots, ACS nano, 7 (2013) 5684-5693.

[151] L. Zhou, Z. Li, Z. Liu, J. Ren, X. Qu, Luminescent Carbon Dot-Gated Nanovehicles for pH-Triggered Intracellular Controlled Release and Imaging, Langmuir, 29 (2013) 6396-6403.

[152] M. Zheng, S. Liu, J. Li, D. Qu, H. Zhao, X. Guan, X. Hu, Z. Xie, X. Jing, Z. Sun, Integrating oxaliplatin with highly luminescent carbon dots: an unprecedented theranostic agent for personalized medicine, Advanced Materials, 26 (2014) 3554-3560.

[153] S.K. Misra, A. Ohoka, N.J. Kolmodin, D. Pan, Next Generation Carbon Nanoparticles for Efficient Gene Therapy, Molecular pharmaceutics, 12 (2015) 375-385.

[154] L. Hu, Y. Sun, S. Li, X. Wang, K. Hu, L. Wang, X.-j. Liang, Y. Wu, Multifunctional carbon dots with high quantum yield for imaging and gene delivery, Carbon, 67 (2014) 508-513.

[155] Q. Wang, X. Huang, Y. Long, X. Wang, H. Zhang, R. Zhu, L. Liang, P. Teng, H. Zheng, Hollow luminescent carbon dots for drug delivery, Carbon, 59 (2013) 192-199.

[156] S. Pandey, M. Thakur, A. Mewada, D. Anjarlekar, N. Mishra, M. Sharon, Carbon dots functionalized gold nanorod mediated delivery of doxorubicin: tri-functional nano-worms for drug delivery, photothermal therapy and bioimaging, Journal of Materials Chemistry B, 1 (2013) 4972-4982.

[157] J. Tang, B. Kong, H. Wu, M. Xu, Y. Wang, Y. Wang, D. Zhao, G. Zheng, Carbon nanodots featuring efficient FRET for real-time monitoring of drug delivery and two-photon imaging, Advanced Materials, 25 (2013) 6569-6574.

[158] J. Kim, J. Park, H. Kim, K. Singha, W.J. Kim, Transfection and intracellular trafficking properties of carbon dot-gold nanoparticle molecular assembly conjugated with PEI-pDNA, Biomaterials, 34 (2013) 7168-7180.

[159] H. Wang, J. Shen, Y. Li, Z. Wei, G. Cao, Z. Gai, K. Hong, P. Banerjee, S. Zhou, Magnetic iron oxide–fluorescent carbon dots integrated nanoparticles for dual-modal imaging, near-infrared light-responsive drug carrier and photothermal therapy, Biomaterials Science, 2 (2014) 915-923.

[160] M.M. Islam, A. Ostadhossein, O. Borodin, A.T. Yeates, W.W. Tipton, R.G. Hennig, N. Kumar, A.C. van Duin, ReaxFF molecular dynamics simulations on lithiated sulfur cathode materials, Physical Chemistry Chemical Physics, 17 (2015) 3383-3393.

[161] A. Ostadhossein, E.D. Cubuk, G.A. Tritsaris, E. Kaxiras, S. Zhang, A.C. van Duin, Stress effects on the initial lithiation of crystalline silicon nanowires: reactive molecular dynamics simulations using ReaxFF, Physical Chemistry Chemical Physics, 17 (2015) 3832-3840.

[162] R. Kumar, W.S. Shin, K. Sunwoo, W.Y. Kim, S. Koo, S. Bhuniya, J.S. Kim, Small conjugate-based theranostic agents: an encouraging approach for cancer therapy, Chemical Society Reviews, (2015).

[163] H.T. Wiogo, M. Lim, V. Bulmus, J. Yun, R. Amal, Stabilization of magnetic iron oxide nanoparticles in biological media by fetal bovine serum (FBS), Langmuir, 27 (2010) 843-850.

[164] R.W. Taylor, T.-C. Lee, O.A. Scherman, R. Esteban, J. Aizpurua, F.M. Huang, J.J. Baumberg, S. Mahajan, Precise subnanometer plasmonic junctions for SERS within gold nanoparticle assemblies using cucurbit [n] uril "glue", ACS nano, 5 (2011) 3878-3887.

[165] J.W. Lee, S. Samal, N. Selvapalam, H.-J. Kim, K. Kim, Cucurbituril homologues and derivatives: new opportunities in supramolecular chemistry, Accounts of chemical research, 36 (2003) 621-630.

[166] Z.-S. Hou, Y.-B. Tan, K. Kim, Q.-F. Zhou, Synthesis, characterization and properties of side-chain pseudopolyrotaxanes consisting of cucurbituril [6] and poly-N 1-(4-vinylbenzyl)-1, 4-diaminobutane dihydrochloride, Polymer, 47 (2006) 742-750.

[167] M. Munteanu, S. Choi, H. Ritter, Cyclodextrin-click-cucurbit [6] uril: Combi-receptor for supramolecular polymer systems in water, Macromolecules, 42 (2009) 3887-3891.

[168] Q. Yang, Y. Jiang, X. Li, Y. Yang, L. Hu, Magnetic-supported cucurbituril: A recyclable adsorbent for the removal of humic acid from simulated water, Bulletin of Materials Science, 37 (2014) 1167-1174.

[169] J. Bartelmess, S. Quinn, S. Giordani, Carbon nanomaterials: multi-functional agents for biomedical fluorescence and Raman imaging, Chemical Society Reviews, (2015).

[170] S. Qu, X. Wang, Q. Lu, X. Liu, L. Wang, A Biocompatible Fluorescent Ink Based on Water-Soluble Luminescent Carbon Nanodots, Angewandte Chemie, 124 (2012) 12381-12384.

[171] J. Kim, I.-S. Jung, S.-Y. Kim, E. Lee, J.-K. Kang, S. Sakamoto, K. Yamaguchi, K. Kim, New cucurbituril homologues: syntheses, isolation, characterization, and X-ray crystal structures

of cucurbit [n] uril (n= 5, 7, and 8), Journal of the American Chemical Society, 122 (2000) 540-541.

[172] W.M. Nau, M. Florea, K.I. Assaf, Deep inside cucurbiturils: physical properties and volumes of their inner cavity determine the hydrophobic driving force for host–guest complexation, Israel Journal of Chemistry, 51 (2011) 559-577.

[173] F. Biedermann, M. Vendruscolo, O.A. Scherman, A. De Simone, W.M. Nau, Cucurbit [8] uril and blue-box: High-energy water release overwhelms electrostatic interactions, Journal of the American Chemical Society, 135 (2013) 14879-14888.

[174] N. Barooah, J. Mohanty, H. Pal, A.C. Bhasikuttan, Cucurbituril-Induced Supramolecular pK a Shift in Fluorescent Dyes and Its Prospective Applications, Proceedings of the National Academy of Sciences, India Section A: Physical Sciences, 84 (2014) 1-17.

[175] A. Praetorius, D.M. Bailey, T. Schwarzlose, W.M. Nau, Design of a fluorescent dye for indicator displacement from cucurbiturils: A macrocycle-responsive fluorescent switch operating through ap K a shift, Organic letters, 10 (2008) 4089-4092.

[176] G. Ghale, V. Ramalingam, A.R. Urbach, W.M. Nau, Determining protease substrate selectivity and inhibition by label-free supramolecular tandem enzyme assays, Journal of the American Chemical Society, 133 (2011) 7528-7535.

[177] N.i. Saleh, Y.A. Al-Soud, L. Al-Kaabi, I. Ghosh, W.M. Nau, A coumarin-based fluorescent PET sensor utilizing supramolecular pK a shifts, Tetrahedron Letters, 52 (2011) 5249-5254.

[178] N.i. Saleh, A.L. Koner, W.M. Nau, Activation and Stabilization of Drugs by Supramolecular pKa Shifts: Drug-Delivery Applications Tailored for Cucurbiturils, Angewandte Chemie, 120 (2008) 5478-5481.

[179] I. Ghosh, W.M. Nau, The strategic use of supramolecular pK a shifts to enhance the bioavailability of drugs, Advanced drug delivery reviews, 64 (2012) 764-783.

[180] A. Jurgeit, R. McDowell, S. Moese, E. Meldrum, R. Schwendener, U.F. Greber, Niclosamide is a proton carrier and targets acidic endosomes with broad antiviral effects, (2012).

[181] Y. G de Paiva, F. da Rocha Ferreira, T. Lucio Silva, E. Labbe, O. Buriez, C. Amatore, M.O. Fonseca Goulart, Electrochemically Driven Supramolecular Interaction of Quinones and Ferrocifens: An Example of Redox Activation of Bioactive Compounds, Current topics in medicinal chemistry, 15 (2015) 136-162.

[182] E. Dede, Ö. Sağlam, Y. Dilgin, Sensitive voltammetric determination of niclosamide at a disposable pencil graphite electrode, Electrochimica Acta, 127 (2014) 20-26.